Electroaeroelastic Analysis and Stability of Galloping-Based Triangular Harvester

By

Umer Javed

2011-NUST-MS PHD- 028

MS-68

Submitted to the Department of Mechanical Engineering in Fulfillment of the Requirements for the Degree of

MASTER OF SCIENCE

in

MECHANICAL ENGINEERING

Thesis Supervisor

Imran Akhtar, Ph.D.

College of Electrical & Mechanical Engineering

National University of Sciences & Technology

2014

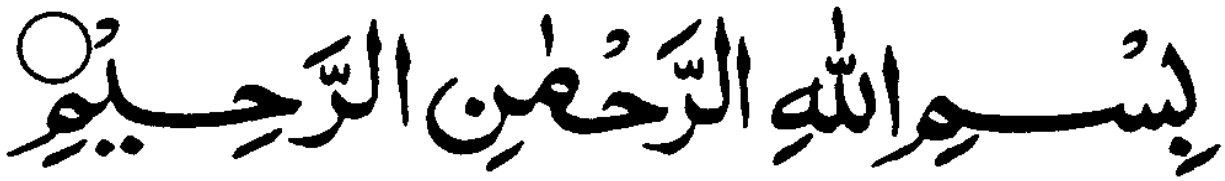

In the name of Allah, the most Beneficent and the most Merciful

Declaration

I hereby declare that I have developed this thesis entirely on the basis of my personal efforts under the sincere guidance of my supervisor Imran Akhtar. All the sources used in this thesis have been cited and the contents of this thesis have not been plagiarized. No portion of the work presented in this thesis has been submitted in support of any application for any other degree of qualification to this or any other university or institute of learning.

_____

Umer Javed

Acknowledgments

Innumerable words of praise and thanks to Allah, the Almighty. Without His Will and Mercy, I would not have been able to accomplish this milestone of my academic career.

I would like to thank my supervisor Dr. Imran Akhtar for his immense guidance, help, and support.

I would like to thank my mentor and guidance committee member Dr. Abdessattar Abdelkefi, an Assistant Professor in the Department of Mechanical and Aerospace Engineering at New Mexico State University, who thoroughly supervised me and guided me in my research. He motivated me and patiently taught me nonlinear dynamics techniques, such as perturbation techniques, normal forms, and shooting method. He helped me through his research methodologies and, approaches. He always encouraged me to ask questions and improve my concepts. I thank him for having confidence in my abilities. He has been a source of inspiration for me.

I would also like to thank my guidance and evaluation committee members Dr. Mazhar Iqbal, Dr. Hasan Aftab Saeed and Assistant Professor Raja Amir Azeem for their continuous support and encouragement. My sincere thanks to Sabir Hussain who always assisted and helped me.

Dedication

To,

My sister *Mrs Asima Amjad*,

My brothers *Abrar Hassan* aka *Asim* and *Haider Javed*

My mentor *Dr. Abdessattar Abdelkefi*

Abstract

With most of the countries using the maximum hydro power they can extract from natural resources, the trend has been shifting towards alternate means. Energy harnessing through vibrating bodies has come out as a very favourable option. Various transduction mechanisms can be used to convert the energy from mechanical vibrations to electrical energy. The ease with which one can get power through environment friendly means and an extremely small setup by volume and cost are the major advantages piezoelectric transduction mechanisms poses. Keeping in mind the changing trends of energy extracting methods, current work focuses on the potential and dynamics of piezoelectric energy harvesting from special class of aero-elastic vibrations called transverse galloping. Different nonlinear dynamics techniques including method of multiple scales and shooting method are used to characterize the harvester's response and determine the contribution of present nonlinearities in the system's response.

Contents

List of Figures

List of Tables

CHAPTER 1

INTRODUCTION

Power crisis overwhelming the world has pushed researchers to show their interests in using natural energy sources such as thermal energy, chemical energy and mechanical energy to generate inexhaustible electrical power. Energy harvesters have paved their ways into our life because of need to power the local electronic devices by using ambient energy. Energy harvesting is for low-power consumption devices, so its usage extends right from powering equipment in remote areas, to giving energy for high-tech equipment in harsh environments. Biomedical field has seen a revolution by inclusion of devices like pacemakers in its arena. Replacement of their batteries by major operations is infeasible and therefore energy harvesters again come into play. Energy harvesters are nowadays used to power micro-electro-mechanical systems (MEMS), health monitoring sensors, wireless sensors, actuators, cameras, cell phones, actuators, etc.

The mechanical energy in the vibrating body can be converted into electrical energy by various transduction mechanisms such as electromagnetic, electrostatic, or piezoelectric. Electric charge accumulates in specialized materials called piezoelectric in response to applied mechanical stress, and the electricity that gets generated is called piezoelectricity. Piezoelectric materials are most popular in MEMS devices because of their easy placement in small volumes. Apart from usage in places requiring small volumes such as MEMS, piezoelectric materials are used to harvest energy from larger mechanisms as well exhibiting sizes greater than MEMS. An advantage that piezoelectric materials have over other energy harnessing mechanisms is that they can convert vibrations into electrical energy over a wide range of frequencies. Piezoelectric

energy harvesters have two modes of operation. They can work in either d_{31} mode or d_{33} mode. The "piezoelectric strain constant" *d* is the ratio of developed free strain to the applied electric field. The subscript d_{ij} indicates that a displacement in the *j* direction will produce an electric charge that will be collected in the *i* direction. In d_{31} mode applied lateral force has direction perpendicular to the polarization direction of the piezoelectric material whereas in d_{33} mode the lateral force has the same direction as that of polarization in the material. Operation of both modes can be seen in Figures 1(a) and 1(b).

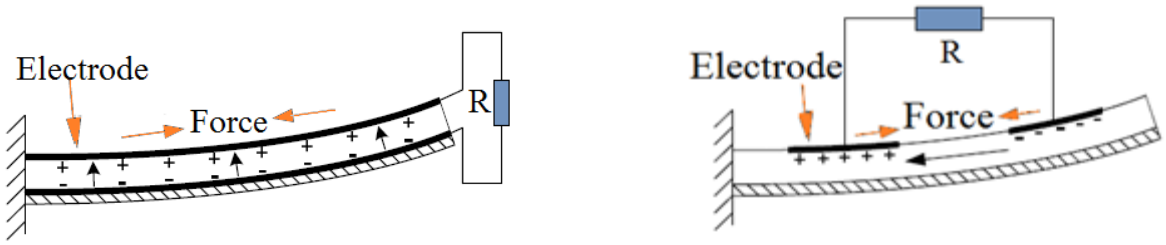

(a) (b)

Figure 1: *The two types of piezoelectric energy harvesters (a) d_{31} mode (b) d_{33} mode.*

Energy harvesting from human movement is of great interest. The kinetic energy from a human body can be translated to produce electrical power that can power wearable electronics like watches or mp3 players, cell phones or even can be used to charge laptops. Upper human body produces movement with frequency around 10 Hz whereas lower body generates movement in the range of 10-30 Hz [1]. SEIKO was the first company to launch prototype of a watch powered by human movement and later successfully launched commercially available watches that were driven on this principle of human movement. Kymissis et al. [2] investigated the concept of harvesting energy from pressure applied on shoes. Energy harvesting from possible backpack motions was studied by Feenstra et al. [3]. They used the piezoelectric option as transducer to convert mechanical energy to its electrical counterpart. They reported that it is possible to harvest 176 μW when considering a 40 lb load on a tread-mill. They also mentioned that 400 μW as a maximum average power can be obtained. In Europe, there are numerous dance clubs that have piezoelectric layers installed [i]. When people dance on the floor their motion

[i] www.artfuldodger.hubpages.com/hub/Piezoelectric-Energy-Harvesting [accessed: 18/7/2014]

causes the generation of electricity via piezoelectric transducers. These amounts of electrical energy are used to charge different types of batteries which can power parts of the nightclub, as shown in Figure 2. Similar concept has been introduced for touch pads where piezoelectric transducers are being placed beneath the LCD touch screen, as presented in Figure 3. When the user touches the screen, an electric charge takes place due to the piezoelectric patch. This electric charge can be used to operate low-power consumption electronics in the touch pad. A survey suggests that PC users use their touch screen around 10000 times a day. This implies that there is a huge potential of using energy by this concept.

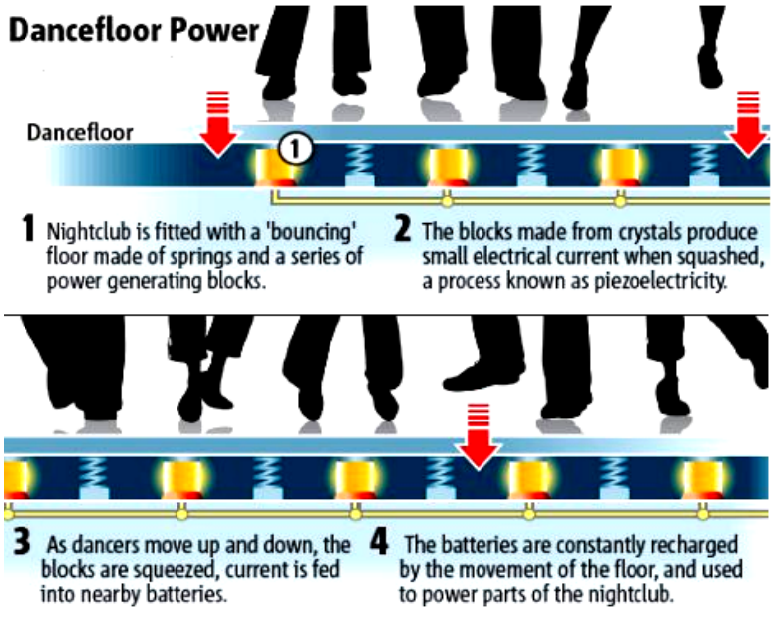

Figure 2: *Concept of dance floor with piezoelectric energy generation* [ii].

Harvesting energy from base vibrations has received the most attention in the past two decades in order to power low-power consumption devices [4-11]. The recent nucleus of attention is generation of electrical power from flow-induced vibrations [12-25]. Wind flowing over an object can cause it to oscillate. These vibrations can cause structure failure and are undesirable for large structures including aircrafts, wind turbines, and pipelines. The trend has shifted to utilize these aeroelastic instabilities to harvest energy in small scale. The transverse galloping

[ii] www.artfuldodger.hubpages.com/hub/Piezoelectric-Energy-Harvesting [accessed: 18/7/2014]

exhibited by bluff bodies is one of those phenomena which is a viable source of energy and is the focus of this Master Thesis.

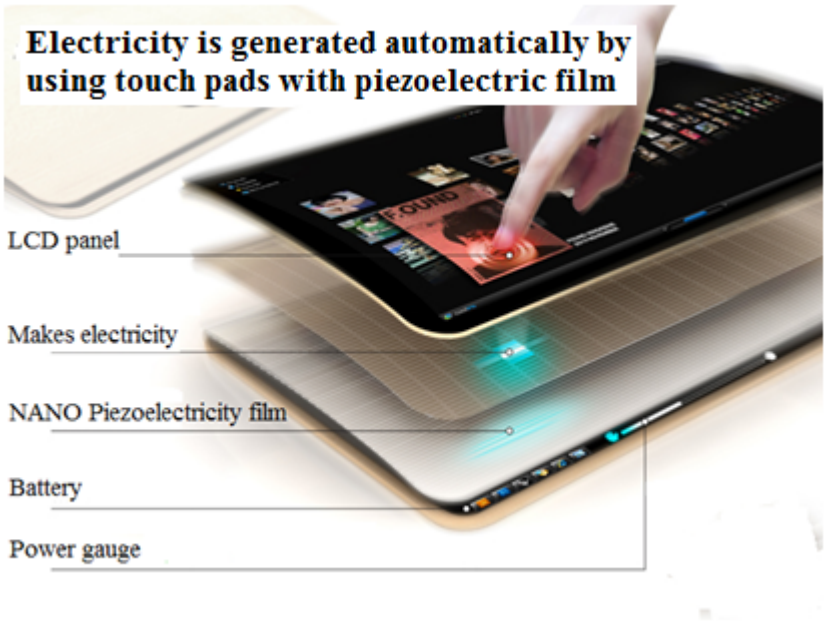

Figure 3: *Concept of touch pad with piezoelectric energy harvesting* [iii].

1.1 Aeroelastic instabilities

As already mentioned, the scope of using piezoelectric energy harvesting by aeroelastic instabilities is increasing. These instabilities exhibit various types: flutter of airfoil sections [12-14], vortex-induced vibrations (VIVs) of circular cylinders [15-17], galloping of prismatic structures (D-section, square, triangular, etc.) [18-23], and wake galloping [24-25]. Flutter is an aerodynamic instability that appears in structures when incoming wind flow increases beyond a critical value. The structural damping therefore becomes insufficient to damp the self-excited motions. Therefore, flutter often leads to catastrophic structure failure. The aircraft wings are designed so as to minimize or control this instability whereas this vulnerability is utilized in case of energy harvesting to design small and efficient energy harvesters. When it comes to VIV, it is entirely different from fluttering. When fluid flows past a bluff body, it produces a von Karman vortex street that consists of chain of vortices on both sides of the body. The alternate shedding

[iii] www.mp4nation.net/blog/2011/05/ecopad-tablet-concept-give-you-power-in-your-touch/ [accessed: 18/7/2014]

of these vortices produces unsteady aerodynamic loads. When the shedding frequency matches the natural frequency of the body, the synchronization or lock-in phenomenon takes place and large transverse oscillations occur. These induced vibrations of the body are referred to as vortex-induced vibrations (VIVs). The schematic of a piezoelectric harvester exhibiting VIV is shown in Figure 4. On the other hand, galloping is a large-amplitude oscillation that is exhibited by prismatic shape cylinders like squares, rectangles, triangles, or D-sections when incoming wind flow exceeds a critical value. When the aerodynamic damping becomes more important than the structural damping, the galloping phenomenon takes place. It should be noted that flutter and galloping exhibit the same dynamics except the fact that galloping oscillations can be obtained by a single-degree-of-freedom.

1.2 Literature review

Anton and Inman [26] performed experiments to investigate the potential of using wing flutter for piezoelectric energy harvesting. They attached piezoelectric material to the wings and concluded that energy harvested can be improved as the size of piezoelectric material is increased. Their results point to an immense potential in fluttering wings for energy harvesting. De Marqui et al. [14] developed a time-domain piezoaeroelastic model of a wing by using piezoceramics. They combined electromechanically coupled finite element model [27] with an unsteady vortex-lattice model [28,29] to represent the aerodynamic loads. A very low aerodynamic damping was observed for low wind velocities and velocities near critical flutter speed. They studied the performance of segmented electrodes and showed that the torsional motions became more effective in the overall dynamics of the system and hence had a direct effect in changing the flutter speed. Abdelkefi et al. [30] modeled a piezoaeroelastic system as a rigid wing which is allowed to move in two degrees of freedom when wind U flows, as shown in Figure 4. They used nonlinear structural stiffness for plunge h and pitch α motions and examined the effect of the electrical load resistance R (across which voltage V gets generated), linear plunge structural stiffness k_h, and linear pitch structural stiffness k_α on the critical flutter speed U_f. They also performed nonlinear analysis by deriving an analytical solution using the normal form of Hopf bifurcation, and compared the results with numerical predictions. They showed

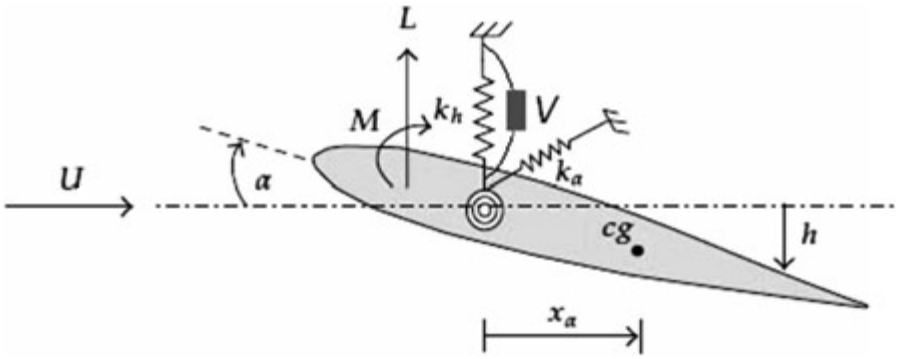

Figure 4: *Schematic of piezoelectric energy harvesting by two degree of freedom of a rigid wing* [iv].

that the nonlinear springs strongly affect the performance of the harvester as well as the type of instability (supercritical or subcritical).

When it comes to VIV, Allen et al. [31] used water tunnel to investigate the behaviour of a flexible membrane placed behind a flat plate. Flow stream normal to the plate created vortices behind the plate, which made the membrane sway from one side to another. When the natural frequency of the membrane matched with the vortex shedding frequency, large amplitude of oscillations exhibited by the membrane pointed to the phenomenon of synchronization. Following this, various researchers used this concept to harness energy from different structures. Wang and Ko [32] successfully produced an instantaneous power of 0.2 μW from an oscillating diaphragm to which a piezoelectric layer had been attached. The oscillating pressure of the water flowing beneath the piezoelectric layer had a pressure of 1.196 kpa with a frequency of 26 Hz that forced the membrane and the piezoelectric layer to vibrate. Abdelkefi et al. [33] discussed the concept of piezoelectric energy harvesting from VIV of circular cylinders, as shown in Figure 5. They used Skop and Griffin model to calculate the lift for the oscillating circular cylinder and coupled the cylinder motion with the harvested voltage by Gauss law. They performed a linear analysis to determine the effects of the electrical load resistance on the coupled frequency of the harvester and associated electromechanical damping. Based on a

[iv] Abdelkefi, A., Nayfeh, A. H., and Hajj, M. R., "Modeling and analysis of piezoaeroelastic energy harvesters," *Nonlinear Dynamics*, Vol. 67, 2012, pp. 925-939.

nonlinear analysis, they reported that a hardening behavior is appeared in the response of the harvester due to the aerodynamic nonlinearity.

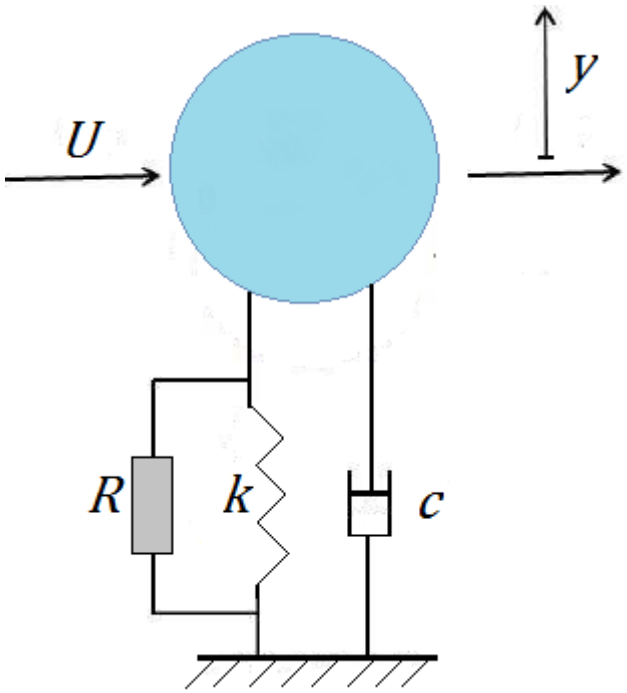

Figure 5: *Concept of piezoelectric energy harvesting by vortex induced vibrations* [v].

Another aeroelastic phenomenon that has shown promise for harvesting energy is the galloping of prismatic structures. There have been studies that have proposed prismatic sections [18,19,34] viable for energy harvesting whereas numerous researches have discussed the effects of various parameters on the galloping of different structures. Sirohi and Mahadik [18] investigated galloping beams with a D-shaped cross section for piezoaeroelastic energy harvesting. Power produced by the harvester was found directly proportional to the incoming wind speed. A wind speed of 5.6 mph was needed to harvest energy from the device. Their results indicated good agreement between their analytical model and experimental data. They

[v] Abdelkefi, A., Hajj, M. R., and Nayfeh, A. H., "Phenomena and modeling of piezoelectric energy harvesting from freely oscillating cylinders," *Nonlinear Dynamics.* Vol. 70, 2012, pp. 1377–88.

reported that quasi-steady approximation for modeling the fluid forces for galloping was sufficient. Afterwards Sirohi and Mahadik [35] considered an equilateral triangle section attached to cantilever beams which had surface bonded piezoelectric sheets. They indicated that this harvester was able to fulfill the need of most of the commercially available wireless sensors. They reported that their analytical model and their experimental results had an inconsistency when it came to the natural frequency and the harvested power. Abdekefi et al. [21] developed a nonlinear distributed-parameter model for galloping-based piezoaeroelastic energy harvesters and validated it with the experimental measurements of Sirohi and Mahadik [35]. Den Hartog [36] was the first one to explain the phenomenon of galloping. He not only used quasi-steady hypothesis to describe the aerodynamic forces on the cylinder, but also developed a criterion for galloping. Barrero et al. [37] in their work have compared the amplitude of oscillations and energy harvesting potential of various prismatic shape cylinders for high Reynolds number flows. Abdelkefi et al. [34] used the Gauss law to couple square cylinder motion with voltage produced. They used Barrero et al. [37] cubic polynomial to analyze a system by performing linear and nonlinear analysis. Their linear analysis revealed a critical wind speed of 4.441m/s, and performed analytical solution by normal form of Hopf bifurcation that matched the numerical predictions. Abdelkefi et al. [19] investigated the effects of different cross-sectional geometries on piezoelectric energy harvesting by transverse galloping. The transducer was attached in the transverse degree of freedom of cylinder. They derived normal form of Hopf bifurcation to characterize the effects of linear and nonlinear parameters on the response of the harvester and to determine the type of Hopf bifurcation the system exhibits for a particular set of parameters. They studied the effects of cross-sectional geometries, electrical load resistance as well as the incoming wind speed on the initiation of galloping as well as harvested power. In another study, Abdelkefi et al. [20] used Euler-Bernoulli beam assumptions to model two different energy harvesting systems: the first one with a tip mass prismatic structure which is attached with a multilayered cantilever beam, whereas the other system consists of equilateral triangle cross section bar that is attached with two cantilever beams. The first system has only aerodynamic whereas the other possesses aerodynamic as well as a structural nonlinearity (nonlinear torsional spring). The dependence of critical value of wind needed for initiation of galloping *i.e.* energy harvesting is analysed for both systems. The normal form is derived for both systems to study the performance and reliability of both harvesters. It was found that the

first system exhibited supercritical Hopf bifurcation for the considered parameters for two different considered cross-sectional geometries. They demonstrated that the electrical load resistance strongly affect the associated nonlinear torsional spring critical value which resulted in a change in the system response from supercritical to subcritical Hopf bifurcation and *vice versa*. Therefore, there is a huge potential of research when it comes to harnessing aeroelastic instabilities, and a continuous contribution is needed.

1.3 Scope of the thesis

1.3.1 Objectives

The objective of this Master Thesis is to investigate the phenomenon of galloping for piezoelectric energy harvesting. We focus on a triangular cylinder galloping with piezoelectric transducer attached in transverse degree of freedom. The effect of structural as well as aerodynamic nonlinearity is studied by developing normal form and numerical predictions. The type of bifurcation is characterized by normal form whereas stability of electroaeroelastic system is analysed by deriving Floquet multipliers.

1.3.2 Thesis contributions

Major contributions of this research include:

1. Developing the normal form of the Hopf bifurcation for a galloping-based energy harvester having both structural and aerodynamic nonlinearities.
2. Deriving the shooting method and comparing its numerical predictions with the normal form of the Hopf bifurcation and Runga-Kutta numerical predictions.
3. Using the shooting method to determine the Floquet multipliers and study the stability of the harvester.

1.4 Outline of the thesis

The thesis is organized as follows:

1. In Chapter 2, we show the importance of method of multiple scales (MMS) and demonstrate its effectiveness when considering various examples.

2. In Chapter 3, we develop the normal form of the Hopf bifurcation for a galloping-based triangular cylinder harvester and validate the results with numerical predictions. We also discuss the effect of the cross-sectional geometry of the cylinder on the onset speed of galloping.
3. In Chapter 4, we derive the shooting method of the considered harvester and discuss, in details, the electroaeroelastic stability of the harvester.
4. In Chapter 5, we summarize and conclude our results. We also present recommendations for future work.

1.5 Summary

We gave an overview of piezoelectric energy harvesting when subjected to base or aeroelastic excitations. The fast rate with which need for localised energy harvesting is increasing is discussed. Different phenomena that harness aeroelastic energy in flowing wind are presented and discussed. A review of aeroelastic energy harvesting during the past few years was done with details. The shift of focus of researchers towards galloping as potential source of energy harvesting was elaborated. At the end, we discussed objectives, contributions, and outline of this Thesis.

CHAPTER 2

METHOD OF MULTIPLE SCALES

2.1 Introduction

In the current chapter, we emphasize the importance of the method of multiple scales, a perturbation method used for finding the analytical solution of dynamical systems. As the name suggests this method scales the time as well as the variables involved in the differential equation. A bookkeeping parameter, generally, denoted as ϵ is used to conserve the scaling. The usefulness of this method lies in the fact that besides predicting steady state solution with reasonable accuracy it captures the transient response of the dynamical system with good precision as well whereas other analytical techniques fail to get the transient portion of the response. We focus on the steps and methodology of this method by considering two simple nonlinear oscillators: 1) self excited Rayleigh oscillator and 2) Duffing oscillator. A brief overview of method of multiple scales, steps and examples presented in this section is discussed in length by Nayfeh [vi] in his book along with other perturbation techniques.

2.1.1 Rayleigh oscillator

In order to demonstrate the effectiveness of this method we consider a second order differential equation with a negative damping in the form of

$$m\frac{d^2u^*}{dt^{*2}} + ku^* = \mu\left[1 - \alpha\left(\frac{du^*}{dt^*}\right)^2\right]\frac{du^*}{dt^*} \qquad \text{(a1)}$$

[vi] Nayfeh, A. H., Introduction to Perturbation Techniques, Wiley, New York, NY, 1993.

where m is the mass of the system, k is the spring coefficient, and μ and α are positive parameters. This equation of motion is called the Rayleigh oscillator. We introduce characteristic displacement as u_0^* and linear natural frequency of the system as $\omega_0 = \sqrt{k/m}$ as the reference quantities and introduce the following dimensionless quantities without the asterisks

$$u = \frac{u^*}{u_0^*},\ t = t^*\sqrt{\frac{k}{m}}$$

Then equation (a1) takes the form

$$\ddot{u} + u = \epsilon\left(1 - \frac{\alpha {u_0^*}^2 k}{m}\dot{u}^2\right)\dot{u} \tag{a2}$$

where $\epsilon = \mu/\sqrt{km}$ and put $\alpha {u_0^*}^2 k = \frac{1}{3}m$ so that equation takes the form

$$\ddot{u} + u = \epsilon\left(\dot{u} - \frac{1}{3}\dot{u}^3\right) \tag{a3}$$

It is important mentioning here that method of multiple scales will be used to solve this form of Rayleigh oscillator in the current section. The time t as well as its derivatives needs to be scaled. The first order time derivative is scaled as shown below

$$\frac{d}{dt} = D_0 + \epsilon D_1 + \cdots \tag{a4}$$

where $D_n = \partial/\partial T_n$. So t is divided into various scales like $T_0 = t$, $T_1 = \epsilon t$, $T_2 = \epsilon^2 t$ which emphasizes the fact that T_0 is a fast time scale, T_1 considerably slower and T_2 even slower than T_1. It should be noted that value of ϵ is kept very small for all analysis of method of multiple scales. Applying the operator $\frac{d}{dt}$ on both sides of equation (a4) reveals

$$\frac{d^2}{dt^2} = D_0^2 + 2\epsilon D_0 D_1 + \cdots \tag{a5}$$

The second-order time derivative used in equation (a3) is given by the above equation (a5). Substituting the values of equations (a4) and (a5) in (a3) gives

$$D_0^2 u + 2\epsilon D_0 D_1 u + u = \in \left[D_0 u - \frac{1}{3}\,(D_0 u)^3\right] + \cdots \tag{a6}$$

We find a solution of u in the form of

$$u = u_0(T_0, T_1) + \epsilon u_1(T_0, T_1) + \cdots \tag{a7}$$

Substituting equation (a7) into equation (a6) and separating the order of ϵ gives

O (ϵ^0)

$$D_0^2 u_0 + u_0 = 0 \tag{a8}$$

O (ϵ^1)

$$D_0^2 u_1 + u_1 = -2D_0 D_1 u_0 + D_0 u_0 - \frac{1}{3}(D_0 u_0)^3 \tag{a9}$$

The equation (a8) gives

$$u_0 = A(T_1)e^{iT_0} + \overline{A}(T_1)e^{-iT_0} \tag{a10}$$

The substitution of equation (a10) into equation (a9) gives the equation

$$D_0^2 u_1 + u_1 = -2iA'e^{iT_0} + 2i\overline{A'}e^{-iT_0} + iAe^{iT_0} - i\overline{A}e^{-iT_0} - \frac{1}{3}\left(iAe^{iT_0} - i\overline{A}e^{-iT_0}\right)^3 \tag{a11}$$

Equation (a11) can then be written as

$$D_0^2 u_1 + u_1 = -i\left(2A' - A + A^2\overline{A}\right)e^{iT_0} + \frac{1}{3}iA^3 e^{3iT_0} + cc \tag{a12}$$

where *cc* represents the complex conjugates of terms.

In order to get a finite response for a dynamical system, we need to remove the secular terms. The removal of these terms requires the coefficient of e^{iT_0} or e^{-iT_0} to be zero. From equation (a12), we have secular term coefficient as

$$2A' - A + A^2\overline{A} = 0 \tag{a13}$$

The solution A of above equation is written in polar form as

$$A = \frac{1}{2}ae^{i\beta} \tag{a14}$$

It should be noted that a and β are real functions of T_1 as evident from equation (a10). The expression of A from equation (a14) makes equation (a10) as

$$u_0 = \frac{1}{2}ae^{i(T_0+\beta)} + \frac{1}{2}ae^{-i(T_0+\beta)} \tag{a15}$$

This equation can be written in the form of

$$u_0 = a\cos(T_0 + \beta) \tag{a16}$$

We substitute equation (a14) into equation (a13), one obtains

$$a'e^{i\beta} + ia\beta'e^{i\beta} - \frac{1}{2}ae^{i\beta} + \frac{1}{8}a^3e^{i\beta} = 0 \tag{a17}$$

Dividing the equation (a17) by $e^{i\beta}$ and separating the real and imaginary parts gives

$$a' = \frac{1}{2}a - \frac{1}{8}a^3 \tag{a18}$$

$$\beta' = 0 \tag{a19}$$

Equation (a19) gives the solution as

$$\beta = \beta_0 = \text{constant} \tag{a20}$$

For equation (a18), we seek separation of variables *i.e.*

$$dT_1 = \frac{8da}{4a-a^3} = \frac{8da}{a(2-a)(2+a)} \tag{a21}$$

The right hand side is represented as partial expressions to give

$$dT_1 = \frac{2da}{a} + \frac{da}{(2-a)} - \frac{da}{(2+a)} \tag{a22}$$

The solution of equation (a22) is in the form of

$$T_1 + c = 2\log a - \log|2-a| - \log(2+a) \tag{a23}$$

The right hand side can be expressed as a single log and equation (a23) takes the following form

$$T_1 + c = \log \frac{a^2}{|4-a^2|} \tag{a24}$$

Removing the log from right hand side makes equation (a24) as

$$\frac{a^2}{4-a^2} = e^{T_1+c} = e^{\epsilon t+c} \tag{a25}$$

Equation (a25) takes the form

$$a^2 = \frac{4\exp(\epsilon t+c)}{1+\exp(\epsilon t+c)} = \frac{4}{1+\exp(-\epsilon t-c)} \tag{a26}$$

Placing the values of β and a^2 from equations (a20) and (a26), respectively, in equation (a16) and we get

$$u_0 = 2[1 + e^{-\epsilon t-c}]^{-1/2} \cos(t + \beta_0) \tag{a27}$$

The expression for u from equation (a7) for first order expansion becomes

$$u = 2\left[1 + \exp\left(-\epsilon t - c\right)\right]^{-1/2}\cos(t + \beta_0) + \cdots \tag{a28}$$

The initial condition for the Rayleigh oscillator *i.e.* equation (a3) is given by

$$u(0) = a_0, \dot{u}(0) = 0 \tag{a29}$$

Substituting equation (a29) into equation (a28) reveals

$$a_0 = 2[1 + e^{-c}]^{-1/2}\cos(\beta_0) \tag{a30}$$

and

$$0 = -2[1 + e^{-c}]^{-1/2}\sin(\beta_0) + O(\epsilon) \tag{a31}$$

Equation (a31) gives $\beta_0 = 0 + O(\epsilon)$ which makes equation (a30) in the form

$$a_0^2 = 4[1 + e^{-c}]^{-1} \tag{a32}$$

Value of e^{-c} from equation (a32) comes out to be

$$e^{-c} = \frac{4}{a_0^2} - 1 \tag{a33}$$

The expression of u from equation (a28) becomes

$$u = 2\left[1 + \left(\frac{4}{a_0^2} - 1\right)e^{-\epsilon t}\right]^{-1/2}\cos(t) + \cdots \tag{a34}$$

The above equation suggests that the steady state solution for equation (a34) becomes

$$u \rightarrow 2\cos t + O(\epsilon) \tag{a35}$$

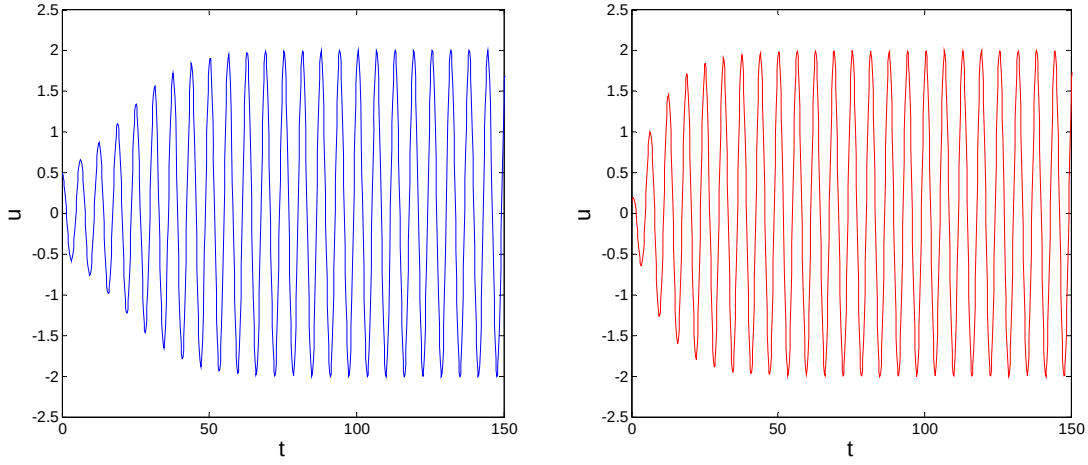

(a) (b)

Figure 6: *Comparison between (a) numerical prediction and (b) analytical solution for* $u(0)$ *=0.5,* $\dot{u}(0) = 0$ *and* ϵ *= 0.1.*

The above value for equation (a35) indicates that as time $t \rightarrow \infty$ the solution u approaches $2cos\,(t)$ irrespective of the value of a_0 as long as $a_0 \neq 0$. Equation (a34) shows that u is not of the form $a\,cos(t + \beta)$ where a is an exponential function of time. The method of multiple scales splits the original differential equation into system of ordinary differential equations and permits enough generality in the solution to obtain an excellent result as evident from comparison with numerical prediction by Runge-Kutta in Figure 6.

2.1.2 Duffing oscillator

The Duffing oscillator is an example of a system having a restoring force in the system. The equation usually called the Duffing equation or oscillator is given by

$$\frac{d^2u^*}{dt^{*2}} + k_1u^* + k_3u^{*3} = 0 \tag{a36}$$

where the $k_1 > 0$ and the nonlinear spring coefficient k_3 may be greater than or less than zero. We consider a characteristic length U^* and characteristic time T^* and let

$$t = \frac{t^*}{T^*} \quad u = \frac{u^*}{U^*} \tag{a37}$$

The chain rule gives

$$\frac{d}{dt^*} = \frac{d}{dt}\frac{dt}{dt^*} = \frac{1}{T^*}\frac{d}{dt} \tag{a38}$$

Applying the operator $\frac{d}{dt^*}$ on both sides of the equation gives

$$\frac{d^2}{dt^{*2}} = \frac{1}{T^{*2}}\frac{d^2}{dt^2} \tag{a39}$$

$\frac{d}{dt^*}$ and $\frac{d^2}{dt^{*2}}$ are substituted in the Duffing equation (a36) to give

$$\ddot{u} + k_1T_1^{*2}u + k_3T^{*2}U^{*2}u^3 = 0 \tag{a40}$$

We choose $k_1T_1^{*2} = 1$ and let $\epsilon = k_3T^{*2}U^{*2} = k_3U^{*2}/k_1$, and therefore equation (a40) can be rewritten as

$$\ddot{u} + u + \epsilon u^3 = 0 \tag{a41}$$

Equation (a41) is the dimensionless form of the Duffing oscillator of equation (a36) and is solved in this section analytically by the method of multiple scales. It should be noted that ϵ is a dimensionless parameter and is a criterion for the strength of nonlinearity. The initial condition for the problem of equation (a41) is given by

$$u(0) = x_0 \qquad \dot{u}(0) = \dot{x}_0 \tag{a42}$$

The solution u is a function of t and ϵ and is given by

$$u(t;\epsilon) = \hat{u}(t, \epsilon t, \epsilon^2 t, \epsilon^3 t, \dots; \epsilon) \tag{a43}$$

$$u(t;\epsilon) = \hat{u}(T_0, T_1, T_2, T_3, \dots; \epsilon) \tag{a44}$$

$$T_0 = t, T_1 = \epsilon t,\ T_2 = \epsilon^2 t,\ T_3 = \epsilon^3 t, \dots \tag{a45}$$

An inspection of equations (a44) and (a45) reveal the fact that t has been divided into various scales. As already discussed time T_0 represents a fast scale, T_1 shows a slow scale whereas T_2 is representative of even a slower scale. The time derivative of the original time t is correspondingly divided into various scales as given below

$$\frac{d}{dt} = \frac{\partial}{\partial T_0} + \epsilon \frac{\partial}{\partial T_1} + \epsilon^2 \frac{\partial}{\partial T_1} + \cdots \tag{a46}$$

Applying the operator $\frac{d}{dt}$ on both sides reveals second order derivative given by

$$\frac{d^2}{dt^2} = \frac{\partial^2}{\partial T_0^2} + 2\epsilon \frac{\partial^2}{\partial T_0 \partial T_1} + \epsilon^2 \left(2 \frac{\partial^2}{\partial T_0 \partial T_2} + \frac{\partial^2}{\partial T_1^2}\right) + \cdots \tag{a47}$$

Substituting values of equations (a46) and (a47) in equation (a41), one obtains

$$\frac{\partial^2 u}{\partial T_0^2} + 2\epsilon \frac{\partial^2 u}{\partial T_0 \partial T_1} + \epsilon^2 \left(2 \frac{\partial^2 u}{\partial T_0 \partial T_2} + \frac{\partial^2 u}{\partial T_1^2}\right) + u + \epsilon u^3 + \cdots = 0 \tag{a48}$$

We scale the non-dimensional response displacement u as

$$u = u_0(T_0, T_1, T_2, \dots) + \epsilon u_1(T_0, T_1, T_2, \dots) + \cdots \tag{a49}$$

Equations (a49) and (a48) give

$$\frac{\partial^2 u_0}{\partial T_0^2} + \epsilon \frac{\partial^2 u_1}{\partial T_0^2} + 2\epsilon \frac{\partial^2 u_0}{\partial T_0 \partial T_1} + u_0 + \epsilon u_1 + \epsilon u_0^3 + \cdots = 0 \tag{a50}$$

For different orders of bookkeeping parameters equation (a50) can be written as

O(ϵ^0)

$$\frac{\partial^2 u_0}{\partial T_0^2} + u_0 = 0 \tag{a51}$$

O(ϵ^1)

$$\frac{\partial^2 u_1}{\partial T_0^2} + u_1 = -2\frac{\partial^2 u_0}{\partial T_0 \partial T_1} - u_0^3 \tag{a52}$$

The solution of u_0 from equation (a51) gives

$$u_0 = a(T_1, T_2, \dots)\cos[T_0 + \beta(T_1, T_2, \dots)]$$

This equation clearly indicates that neither a nor β are functions of fast time scale T_0. Moreover as $cos(\theta) = \frac{1}{2}\left(e^{i\theta} + e^{-i\theta}\right)$, therefore the above equation can be written as

$$u_0 = \frac{1}{2}a[e^{i(T_0+\beta)} + e^{-i(T_0+\beta)}] \tag{a53}$$

$$= \frac{1}{2}[ae^{i(T_0+\beta)} + ae^{-i(T_0+\beta)}]$$

$$= \frac{1}{2}ae^{i\beta}e^{iT_0} + \frac{1}{2}ae^{-i\beta}e^{-iT_0}]$$

$$u_0 = Ae^{iT_0} + \bar{A}e^{-iT_0} \tag{a54}$$

where

$$A = \frac{1}{2}ae^{i\beta} \tag{a55}$$

The value of u_0 from equation (a54) is substituted in equation (a52) to get

$$\frac{\partial^2 u_1}{\partial T_0^2} + u_1 = -2i\frac{\partial A}{\partial T_1}e^{iT_0} + 2i\frac{\partial \bar{A}}{\partial T_1}\,e^{-iT_0} - (Ae^{iT_0} + \bar{A}e^{-iT_0})^3 \tag{a56}$$

which gives

$$\frac{\partial^2 u_1}{\partial T_0^2} + u_1 = -\left(2i\frac{\partial A}{\partial T_1} + 3A^2\bar{A}\right)e^{iT_0} + \left(2i\frac{\partial \bar{A}}{\partial T_1} - 3\overline{A^2}A\right)e^{-iT_0} - A^3e^{3iT_0} - \overline{A^3}e^{-3iT_0} \tag{a57}$$

As already discussed e^{iT_0} and e^{-iT_0} produce secular terms in the system of equations and should be removed for a finite response to appear therefore

$$2i\frac{\partial A}{\partial T_1} + 3A^2\bar{A} = 0 \tag{a58}$$

$$2i\frac{\partial \bar{A}}{\partial T_1} - 3\overline{A^2}A = 0 \tag{a59}$$

Equations (a58) and (a59) are complex conjugates and considering only one of them can serve the purpose. Therefore, substituting equation (a55) into equation (a58), we obtain

$$2i\left(\frac{1}{2}\frac{\partial a}{\partial T_1}e^{i\beta} + \frac{1}{2}ai\frac{\partial \beta}{\partial T_1}e^{i\beta}\right) + 3.\frac{a^2}{4}e^{2i\beta}.\frac{a}{2}e^{-i\beta} = 0 \tag{a60}$$

Simplifying the previous equation gives

$$i\frac{\partial a}{\partial T_1}e^{i\beta} - a\frac{\partial \beta}{\partial T_1}e^{i\beta} + \frac{3}{8}a^3e^{i\beta} = 0 \tag{a61}$$

$$i\frac{\partial a}{\partial T_1} - a\frac{\partial \beta}{\partial T_1} + \frac{3}{8}a^3 = 0 \tag{a62}$$

Separating the real and imaginary parts from equation (a62) gives

$$\frac{\partial a}{\partial T_1} = 0 \tag{a63}$$

$$a\frac{\partial \beta}{\partial T_1} - \frac{3}{8}a^3 = 0 \tag{a64}$$

Then, the particular solution of equation (a57) is given by

$$u_1 = \frac{1}{32}a^3\cos(3T_0 + 3\beta) \tag{a65}$$

and equation (a64) gives

$$\frac{\partial \beta}{\partial T_1} = \frac{3}{8}a^2 \tag{a66}$$

and β comes out to be

$$\beta = \frac{3}{8}a^2 T_1 + \beta_0(T_2, T_3, \dots) \tag{a67}$$

Equation (a63) implies that a is not a function of time T_1 therefore we have

$$a = a(T_2, T_3, \dots) \tag{a68}$$

After substituting values of u_0 and u_1, the response u (equation (a49)) of the Duffing oscillator represented by equation (a41) gets the form as shown below

$$u = acos(T_0 + \beta) + \frac{1}{32}\epsilon a^3 \cos(3T_0 + 3\beta) + \cdots \tag{a69}$$

Equations (a67), (a68), and (a69) give

$u = a(T_2, T_3, \dots)cos\left[T_0 + \frac{3}{8}T_1 a^2(T_2, T_3, \dots) + \beta_0(T_2, T_3, \dots)\right] + \frac{1}{32} \in a^3(T_2, T_3, \dots)\cos\Big[3T_0 +$
98T1a2T2,T3,…+3β0T2,T3,…+…

Putting the original time t and neglecting higher powers of ϵ, we have

$$a(T_2, T_3, \dots) = a(\epsilon^2 t, \epsilon^3 t, \dots)$$
$$= a(0,0, \dots) + \frac{\partial a}{\partial T_2}\epsilon^2 t + \cdots$$
$$= \hat{a} + O(\epsilon^2 t)$$

Similar process for β_0 gives

$$\beta_0(T_2, T_3, \dots) = \beta_0(\epsilon^2 t, \epsilon^3 t, \dots)$$
$$= \beta_0(0,0, \dots) + \frac{\partial \beta_0}{\partial T_0}\epsilon^2 t + \cdots$$
$$= \hat{\beta}_0 + O(\epsilon^2 t)$$

We get non-dimensional displacement u as

$$u = \hat{a}\cos(T_0 + \frac{3}{8}T_1\hat{a}^2 + \beta_0) + \frac{1}{32}\epsilon\hat{a}^3\cos\left(3T_0 + \frac{9}{8}T_1\hat{a}^2 + 3\hat{\beta}_0\right) + O(\epsilon^2 t)$$
$$u = \hat{a}\cos(t + \frac{3}{8}\epsilon t\hat{a}^2 + \hat{\beta}_0) + \frac{1}{32}\epsilon\hat{a}^3\cos\left(3t + \frac{9}{8}\epsilon t\hat{a}^2 + 3\hat{\beta}_0\right) + O(\epsilon^2 t)$$

$$u = \hat{a}\cos\left(t + \frac{3}{8}\epsilon t\hat{a}^2 + \hat{\beta}_0\right) + O(\epsilon)$$

A comparison between analytical solution from method of multiple scales and numerical prediction is given for Duffing oscillator in Figure 7 and it can be seen that analytical approximation is in excellent agreement with numerical prediction by Runge-Kutta.

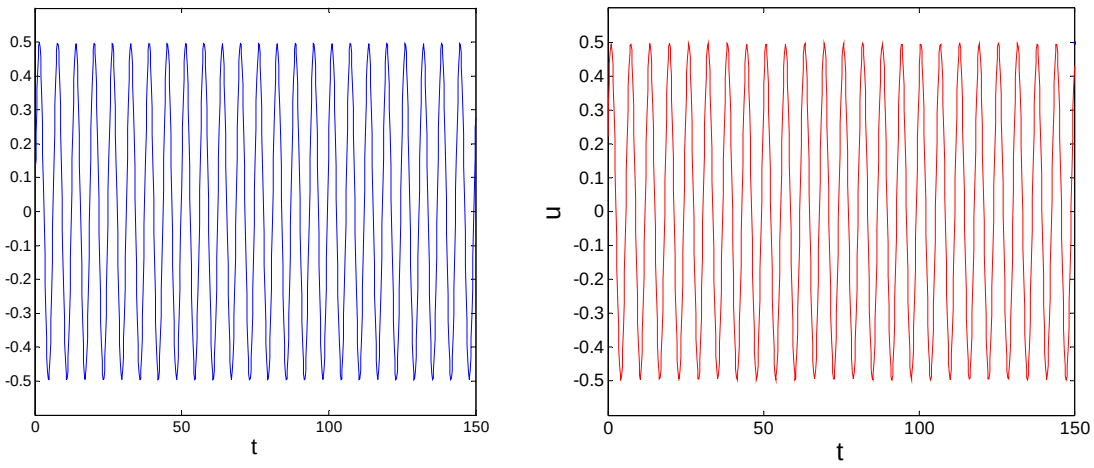

(a) (b)

Figure 7: *Comparison between (a) numerical prediction and (b) analytical solution for* $u(0) = 0$, $\dot{u}(0) = 0.5$ *and* $\epsilon = 0.1$.

2.2 Summary

This chapter elaborated the importance of a perturbation method when using the method of multiple scales for analytical prediction of dynamical systems. Two different oscillators were considered and analytical solutions are provided when using the method of multiple scales for both systems. After that, comparisons were performed between the obtained analytical and numerical predictions. It was observed that analytical solutions were in excellent agreement with the numerical predictions.

Chapter 3

ENERGY HARVESTING OF A GALLOPING PIEZOELECTRIC ENERGY HARVESTER

3.1 Introduction

To operate self-powered sensors, actuators, and other electronic devices, various types of wasted natural energy including thermal [38,39], light [40], and kinetic energy [41,42] have been used to generate inexhaustible electrical energy. Such energy harvesters have been proposed to replace small batteries that have a finite life span or would require expensive and time consuming maintenance. For powering electronic devices, mechanical energy has received significant attention in the last decade. Harvesting mechanical energy through converting vibrations to electrical energy can be achieved using either electrostatic [43], electromagnetic [41,44], magnetostrictive [45], or piezoelectric [4,41,9] transduction mechanisms. Of these mechanisms, the piezoelectric option has received the most attention because of its ease of application, non-reliance on input voltage, it can effectively be placed in small volumes, and it can harvest energy over a wide range of frequencies.

For the purpose of piezoelectric energy harvesting, two major ambient excitation categories have been considered which are base [4,41,9] and flow-induced [30,19,20,21,36,26] vibrations. To date, most of the proposed energy harvesting devices from mechanical vibrations have concentrated on exploiting base vibrations. More recently, several research studies have

focused on the concept of energy harvesting from aeroelastic or flow-induced vibrations, such as flutter of airfoil sections [12,14], vortex-induced vibration (VIV) of circular cylinders [15-17], galloping of prismatic structures [18-23], and wake galloping of parallel cylinders [24,25].

Due to its design simplicity compared to the flutter and VIV-based energy harvesters, recent research studies have focused on the concept of energy harvesting from transverse galloping oscillations of prismatic structures. This phenomenon occurs when the wind speed exceeds a critical value and hence the bluff body starts to oscillate [36]. It is well-known that the galloping phenomenon is accompanied by a Hopf bifurcation which can be supercritical or subcritical. In the supercritical case, the harvester has only stable solutions for wind speed values larger than the onset speed of galloping. On the other hand, unstable solutions are present in the subcritical cases for wind speed values smaller than the onset speed of galloping. The presence of these unstable solutions are dependent on the initial condition (IC) values. To characterize the type of instability and determine the unstable solutions, two different approaches are used, namely, the normal form of the Hopf bifurcation and the Floquet multipliers obtained from the shooting method used for the construction of periodic solutions. In this work, structural and aerodynamic nonlinearities are present. The aerodynamic nonlinearity is associated to the galloping force and is defined by the flow parameters and the properties of the prismatic structure. As for the structural nonlinearity, hardening or softening springs can be used. The rest of this chapter is organized as follows: In Section 3.2, a lumped-parameter model representing the dynamics of the harvester is presented. A linear stability analysis is then performed, in Section 3.3, to determine the onset speed of galloping of the harvester. In Section 3.4, the normal form of the Hopf bifurcation is derived to characterize the type of instability and determine the contributions of the aerodynamic and structural nonlinearities on the performance of the harvester. In addition, the shooting method is used to construct the periodic solutions and determine the Floquet multipliers to characterize their stability.

3.2 Electro-aeroelastic model formulation

A galloping-based aeroelastic energy harvester is considered. This harvester consists of a tip mass isosceles triangular section $\delta = 30^o$ attached to a multilayered cantilever beam, as shown in Figure 8. The multilayered beam is composed of substrate and piezoelectric layers. The piezoelectric layer is bonded by two-in-plane electrodes of negligible thicknesses connected to

an electrical load resistance R. When subjected to an incoming flow, this harvester can undergo galloping oscillations in the transverse direction. The Den Hartog stability criterion [36] states that a section of a bluff body on a flexible support is susceptible to galloping when the linear term associated with the speed of the aerodynamic galloping force is positive. For the harvester under investigation, the onset speed of galloping is determined when the electro-mechanical damping of the harvester changes sign from a positive to a negative value due to the aerodynamic galloping force. The nonlinear term of the galloping force affects the amplitude of the ensuing limit-cycle oscillations and hence the level of the harvested power.

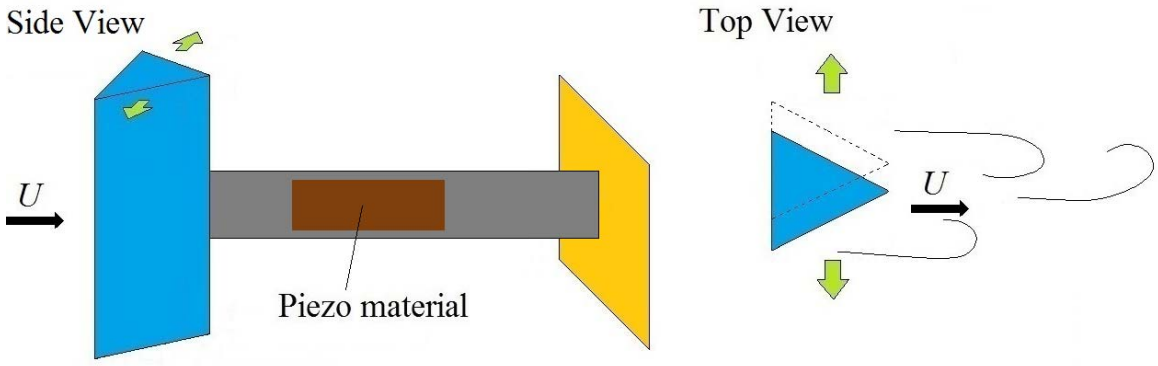

Figure 8: *Schematic of the galloping triangular cylinder ($\delta = 30^o$) for piezoelectric energy harvesting.*

In this work, a lumped-parameter model is used to express the governing equations of the coupled electro-mechanical system which are given by

$$m\left(\ddot{y} + 2\xi\omega_n\dot{y} + \frac{k}{m}y\right) - \theta V = F_y = \frac{1}{2}\rho U^2 D C_y \tag{1}$$

$$C_p\dot{V} + \frac{V}{R} + \theta\dot{y} = 0 \tag{2}$$

where y is the cylinder displacement, $\dot{y}$ is the cylinder velocity, V is the generated voltage across the electrical load resistance R, m is the total mass per unit length, k is the system's stiffness per unit length, ξ is the mechanical damping ratio, is the cylinder natural frequency, θ is the electro-

mechanical coupling coefficient, C_p is the capacitance of the piezoelectric layer, ρ is the incoming fluid density, U is the speed of incoming flow, D is the characteristic dimension of the body normal to the incoming flow, F_y and C_y represent, respectively, the galloping force per unit length and force coefficient in the normal direction to the incoming flow. It should be noted that a nonlinear representation of the stiffness of the system is considered. This structural nonlinearity can be due to a nonlinear torsional spring in the clamped side of the harvester [18,21] or due to the beam's geometric or inertia nonlinearities.

$$k = k_0 + k_2 y^2 \tag{3}$$

where k_0 is the linear spring coefficient given by $k_0 = m\omega_n^2$ and k_2 is the nonlinear spring coefficient. The aerodynamic force F_y is modeled by using the quasi-steady approximation [37]. This assumption is justified by the fact that, in transverse galloping, the characteristic time scale of the structure oscillation is much larger than the characteristic time scale of the flow. In addition, the vortex-shedding frequency is much larger than the natural frequency of the harvester. The aerodynamic force per unit length F_y is directly related to the lift and drag coefficients F_y and C_d by

$$F_y = -\frac{1}{2}\rho U^2 D\,[C_l cos(\alpha) + C_d sin(\alpha)] \tag{4}$$

where α is the angle of attack which is given by $\alpha = \tan^{-1}\frac{\dot{y}}{U}$.

For applications where Reynolds number is relatively high, Barrero et al. [37] showed that the galloping force can be approximated by a cubic polynomial representation of $\tan(\alpha)$ in the form

$$F_y = -\frac{1}{2}\rho U^2 D\,[a_1 tan(\alpha) + a_3 tan^3(\alpha)] \tag{5}$$

where a_1 and a_3 are empirical coefficients that are determined by fitting Cy with a polynomial of $tan(\alpha)$. For the considered isosceles triangle ($\delta = 30^o$) the linear and nonlinear coefficients $a_1$and a_3 of the galloping force are determined by Parkinson and Smith [46] and Barrero et al. [37] and are equal to 2.9 and -6.2, respectively.

Considering $\alpha = \tan^{-1}\frac{\dot{y}}{U}$ the galloping force can be expressed as

$$F_y = \frac{1}{2}\rho U^2 D[a_1\frac{\dot{y}}{U} + a_3\left(\frac{\dot{y}}{U}\right)^3] \quad (6)$$

In this considered harvester, we set $m = 4.4\ kg$, $\xi = 0.013$, $\omega = 6.283$ rad/s, $\theta = 1.55\times 10^{-3}$, $\rho = 1.25\ kg/m^3$, $D = 1.5\times 10^{-1}\ m$, $C_p = 1.2\times 10^{-7}$

3.3 Linear stability analysis

The galloping phenomenon takes place when the electro-mechanical damping of the harvester changes sign from positive to negative value due to the aerodynamic force. The wind speed at which the electro-mechanical damping is zero corresponds to the onset of linear instability and is termed the onset speed of galloping, U_g.

To determine this onset speed of galloping and its relation to the electrical load resistance, a linear stability analysis is performed. To this end, we introduce the following state variables

$$\mathbf{X} = \begin{bmatrix} X_1 \\ X_2 \\ X_3 \end{bmatrix} = \begin{bmatrix} y \\ \dot{y} \\ V \end{bmatrix} \quad (7)$$

The coupled electromechanical dynamical system is represented in state space as

$$\dot{X}_1 = X_2 \quad (8)$$

$$\dot{X}_2 = -\left(2\xi\omega_n - \frac{\rho U D a_1}{2m}\right)X_2 - \omega^2 X_1 + \frac{\theta}{m}X_3 + \frac{\rho D a_3}{2mU}X_2^3 - \frac{k_2}{m}X_1^3 \quad (9)$$

$$\dot{X}_3 = -\frac{1}{RC_p}X_3 - \frac{\theta}{C_p}X_2 \quad (10)$$

Clearly, these governing equations can be expressed in the following vector form

$$\dot{\boldsymbol{X}} = B\boldsymbol{X} + \mathbf{C}(\mathbf{X}, \mathbf{X}, \mathbf{X}) \quad (11)$$

where

$$B = \begin{bmatrix} 0 & 1 & 0 \\ -{\omega_n}^2 & -\left(2\xi\omega_n - \frac{\rho U D a_1}{2m}\right) & \frac{\theta}{m} \\ 0 & -\frac{\theta}{C_p} & -\frac{1}{RC_p} \end{bmatrix}$$

The nonlinear vector $\mathbf{C}(\mathbf{X}, \mathbf{X}, \mathbf{X})$, it is given by $\mathbf{C}^T = \left[0, \quad \frac{\rho D a_3}{2mU_g} X_2^3 - \frac{k_2}{m} X_1^3, \quad 0\right]$. It should be noted that the eigenvalues of the linear state space matrix B reveal the onset of instability or galloping of the dynamical system. A structural galloping system usually consists of two eigenvalues in the form of a pair of complex conjugates $\lambda_1 = \lambda_2$. Including the piezoelectric effect in the transverse degree of freedom of the galloping system results in the presence of another eigenvalue λ_3, which is always real and negative and is independent of the incoming wind speed U. The real part of λ_1 or λ_2 represents the damping coefficient and is dependent on the incoming wind speed, whereas the complex part represents the global frequency of the coupled dynamical system. Therefore, the linear stability of the trivial solution depends only on the real part of the first two eigenvalues. Any wind speed which is less than a critical threshold is insufficient to get galloping oscillations and hence a negative real part of the complex conjugates agrees with this fact. The wind speed that makes the real part of λ_1 zero corresponds to the onset of instability. Likewise, wind speed larger than U_g will be sufficient to initiate the phenomenon of galloping which corresponds to a positive real part of the complex conjugates of the dynamical system.

Inspecting matrix B, it is clear that the onset speed of galloping U_g is dependent on the electrical load resistance value, as shown in Table 1 and Figure 9. We present, in this table, the values of the onset speed of galloping for various values of the electrical load resistance. Clearly, maximum values of the onset speed of galloping are obtained for load resistance values around 10^6. We should mention that these maximum onset speed of galloping values are associated with maximum values of the electro-mechanical damping.

Table 1: Critical value of incoming wind velocities for various resistances

$R\ (\Omega)$	U_g
10^3	2.6526
10^4	2.7321
10^5	3.5224
10^6	8.1915
1.5×10^6	8.2506
10^7	4.0181

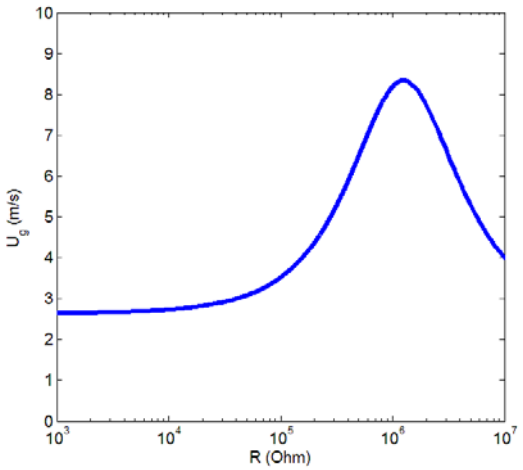

Figure 9: *Variation of the onset of instability U_g with resistance R for triangular cylinder $\delta = 30^o$.*

3.4 Nonlinear characterization of the system's response

In the present system undergoing codimension-one bifurcation, the wind speed is the control parameter. In addition to the conditions implying that the fixed point undergoing the bifurcation is a nonhyperbolic fixed point, the transversality condition is also satisfied. Because the real part

of $\frac{d\lambda_1}{dU}$ is non-zero at U_g, the instability associated with the galloping phenomenon is a Hopf bifurcation. Clearly, the type of this Hopf bifurcation can be supercritical or subcritical. The supercritical type is known by the presence of stable solutions for wind speed values larger than the onset speed of galloping. When $U < U_g$, no oscillations are obtained. We should mention that the limit-cycle oscillations associated with the supercritical Hopf bifurcation are independent of the IC. On the other hand, the subcritical Hopf bifurcation is known by the presence of unstable solutions for wind speed values smaller than the onset speed of galloping. These unstable solutions are dependent on the IC values. In this section, a particular focus will be paid to characterize the type of instability and determine the unstable solutions. To this end, the nonlinear normal form and the shooting methods are used. The nonlinear normal form is derived to characterize the type of instability and to determine the influence of structural and aerodynamic nonlinearities on the performance of the harvester. The shooting method is used to construct the periodic solutions by treating the initial-value problem as a boundary-value problem. Thus, we determine the unstable solutions for subcritical cases by computing the Floquet multipliers which give a clear idea on the stability of the harvester.

3.4.1 Nonlinear normal form

The normal form of the Hopf bifurcation is derived to determine the level of the harvested power and its dependence to the harvester's parameters. More importantly, this nonlinear normal form is used to characterize the type of ensuing instability or bifurcation. To this end, the following perturbation term $\epsilon^2\sigma_U U_g$ is added to the onset speed of galloping and hence the wind speed the wind speed is expressed as $U = U_g + \epsilon^2\sigma_U U_g$, where $\sigma_U = \frac{U-U_g}{U_g}$. The presence of this perturbation term leads to the appearance of the secular terms at the third order approximation. Using this expansion, the matrix $B(U)$ is rewritten as

$$B(U) = B(U_g) + \epsilon^2\sigma_U B_1(U_g)$$

where

$$B_1(U_g) = \begin{bmatrix} 0 & 0 & 0 \\ 0 & \frac{\rho U_g Da_1}{2m} & 0 \\ 0 & 0 & 0 \end{bmatrix}$$

Equation (11) can be expressed as

$$\dot{\mathbf{X}} = B(U_g)\mathbf{X} + \epsilon^2 \sigma_U B_1(U_f)\mathbf{X} + \mathbf{C}(\mathbf{X}, \mathbf{X}, \mathbf{X}) \tag{12}$$

where

$$\mathbf{C}^T = \begin{bmatrix} 0 & \frac{\rho Da_3}{2mU_g} X_2^3 - \frac{k_2}{m} X_1^3 & 0 \end{bmatrix}$$

Letting G be the matrix whose columns are the eigenvectors of the matrix $B(U_g)$ corresponding to the eigenvalues $\pm j\omega_g$ and $-\mu_3$ and defining a new vector $\mathbf{Y}$ such that $\mathbf{X} = G\mathbf{Y}$, equation (12) can be rewritten as

$$G\dot{\mathbf{Y}} = B(U_f)G\mathbf{Y} + \epsilon^2 \sigma_U B_1(U_f)G\mathbf{Y} + \mathbf{C}(G\mathbf{Y}, G\mathbf{Y}, G\mathbf{Y}) \tag{13}$$

Multiplying equation (13) from the left by the inverse G^{-1} of G yields

$$\dot{\mathbf{Y}} = J\mathbf{Y} + \epsilon^2 \sigma_U KG\mathbf{Y} + G^{-1}\mathbf{C}(G\mathbf{Y}, G\mathbf{Y}, G\mathbf{Y}) \tag{14}$$

where $K = G^{-1}B_1(U_f)G$ and $J = G^{-1}B(U_f)G$ is a diagonal matrix whose elements are the eigenvalues $\pm j\omega_g$ and $-\mu_3$. It is clear that $Y_2 = \overline{Y_1}$ Therefore, in component form, equation (14) can be expressed as

$$\dot{Y}_1 = j\omega_1 Y_1 + \sigma_U \sum_1^3 K_{1i} Y_i + N_1(\boldsymbol{Y}) \tag{15}$$

$$\dot{Y}_3 = -\mu_3 Y_1 + \sigma_U \sum_1^3 K_{3i} Y_i + N_3(\boldsymbol{Y}) \tag{16}$$

where the $N_i(Y)$ are tri-linear functions of the components of $\mathbf{Y}$.

The present structural and aerodynamic nonlinearities in the equations of motion are cubic. Hence, the solution of Y_3 decays to zero and only the solution (Y_1) is non-decayed. To compute the nonlinear normal form, we follow Nayfeh and Balachandran [47] and Abdelkefi and Ghommem [48] and search for a third-order approximate solution of equation (15) in the following form

$$Y_1 = \epsilon Y_{11}(T_0, T_2) + \epsilon^2 Y_{12}(T_0, T_2) + \epsilon^3 Y_{13}(T_0, T_2) + O(\epsilon^4) \tag{17}$$

where $T_n = \epsilon^n t$. The time derivative is expressed, in terms of the T_i, as

$$\frac{d}{dt} = \frac{\partial}{\partial T_0} + \epsilon^2 \frac{\partial}{\partial T_2} = D_0 + \epsilon^2 D_2 \tag{18}$$

Substituting the approximated solution of Y_1 in equation (15), new equations have been obtained by satisfying the coefficients of like powers of ϵ. Using this strategy, two different set of equations corresponding to ϵ and ϵ^3 are obtained:

O (ϵ)

$$D_O Y_{11} - j\omega_g Y_{11} = 0 \tag{19}$$

$O(\epsilon^3)$

$$D_O Y_{13} - j\omega_g Y_{13} = -D_2 Y_{11} + \sigma_U (K_{11} Y_{11}) + N(Y_{11} Y_{11} \overline{Y_{11}}) + cc + NST \tag{20}$$

where *NST* stands for terms that do not produce secular terms and cc stands for the complex conjugate of the preceding terms. The solution of equation (19) can be expressed as

$$Y_{11} = A(T_2)\left(e^{j\omega_g T_O}\right) \tag{21}$$

Then, we substitute equation (21) into equation (20) and eliminate the terms that lead to secular terms, we obtain the following modulation equation

$$D_2 A = \beta A + \alpha_e A^2 \bar{A} \tag{22}$$

where $\beta = \sigma_U K_{11}$ and α_e is the effective nonlinearity which is a function of the system parameters, including the electrical load resistance and the linear and nonlinear coefficients a_1, a_3, and k_2.

Letting $A(T_2) = \frac{1}{2} a e^{i\gamma\,(T_2)}$ and separating the real and imaginary parts in equation (22), we obtain the normal form of the Hopf bifurcation:

$$\acute{a} = \beta_r a + \frac{1}{4}\alpha_{er} a^3 \tag{23}$$

$$\acute{\gamma} = \beta_i + \frac{1}{4}\alpha_{er} a^3 \tag{24}$$

where a is the amplitude, γ is the shifting angle of the periodic solution, β_r = Real (β), and α_{er} = Real (α). Equation (23) has three equilibrium solutions which are given by

$$a = 0, a = \pm\sqrt{\frac{-4\beta_r}{\alpha_{er}}}$$

Table 2: Values of the real parts of β and α_{er} and the critical value of the structural spring k_2 for different values of load resistance

$R\ (\Omega)$	β_r	α_{er}	$k_2^{cr}\ (N/m^3)$
10^3	$0.082\ \sigma_U$	$3.5 \times 10^{-3} a_3 - 2.65 \times 10^{-22} k_2$	-8.23×10^{19}
10^4	$0.084\ \sigma_U$	$4.8 \times 10^{-5} a_3 + 2.81 \times 10^{-13} k_2$	1.07×10^9
10^5	$0.109\sigma_U$	$3.8 \times 10^{-7} a_3 + 2.81 \times 10^{-12} k_2$	837961
10^6	$0.260\sigma_U$	$2.65 \times 10^{-9} a_3 + 1.79 \times 10^{-11} k_2$	918.39
1.5×10^6	$0.262\sigma_U$	$1.74 \times 10^{-9} a_3 + 1.77 \times 10^{-11} k_2$	603.28
10^7	$0.124\sigma_U$	$2.13 \times 10^{-9} a_3 + 3.96 \times 10^{-12} k_2$	3338.27

The zero equilibrium solution $a = 0$ corresponds to the fixed point (0,0). The other two solutions are the nontrivial ones. The origin is asymptotically stable for $\beta_r < 0$ or $\beta_r = 0$ and $\alpha_{er} < 0$, unstable for $\beta_r > 0$ or $\beta_r = 0$ and $\alpha_{er} > 0$. Concerning the nontrivial solutions, they exist when $\beta_r \alpha_{er} < 0$. These nontrivial solutions are stable (supercritical Hopf bifurcation) for $\beta_r > 0$ and $\alpha_{er} < 0$ and unstable (subcritical Hopf bifurcation) for $\beta_r < 0$ and $\alpha_{er} > 0$. In

terms of designing efficient and reliable galloping-based aeroelastic energy harvesters, the real part of the effective nonlinearity α_{er} should be the closest possible to zero and negative to guarantee maximum values of the harvested power with a supercritical Hopf bifurcation.

Considering $a_1 = 2.9$ for the considered isosceles triangle ($\delta = 30^0$) cross-sectional geometry, we present in Table 2 the values of β_r and α_{er} for different values of the electrical load resistance. Clearly, the real part of the effective nonlinearity (α_{er}) directly depends on the nonlinear structural and aerodynamic nonlinearities (a_3 and k_2). Inspecting this table, it is noted that a variation in the value of the load resistance is accompanied by a variation in β_r and α_{er}. This significant dependence of the real part of the effective nonlinearity to the electrical load resistance results in a significant change in the critical value of nonlinear structural spring (k_2^{cr}). This critical value is associated to the instability change from a subcritical Hopf bifurcation to a supercritical one and *vice versa*. This significant change in the critical value of the structural spring is associated to the significant dependence of the onset speed of galloping to the electrical load resistance, as shown in Table 1.

It follows from Table 1 that higher onset speed of galloping values which are for $R = 10^6\ \Omega$ and $R = 1.5 \times 10^6\ \Omega$ are accompanied with minimum values of the critical nonlinear structural spring (k_2^{cr}). Furthermore, when $R = 10^3\ \Omega$, a softening nonlinear spring ($k_2 < 0$) is needed to change the system's behavior from a supercritical instability ($\alpha_{er} < 0$) to a subcritical one ($\alpha_{er} > 0$). For this load resistance value, k_2 has to be smaller than the critical value of the structural spring k_2^{cr}. For the rest considered values of the load resistance, the structural spring k_2 has to be larger than its critical value k_2^{cr} to change the instability from supercritical to subcritical one. Using the normal form of the Hopf bifurcation, the displacement of the triangular cylinder y, generated voltage V, and harvested power P can be obtained as follows:

$$y = a\sqrt{G[1,1]_r^2 + G[1,1]_i^2} \tag{25}$$

$$V = a\sqrt{G[3,1]_r^2 + G[3,1]_i^2} \tag{26}$$

$$P = \frac{V^2}{R} \tag{27}$$

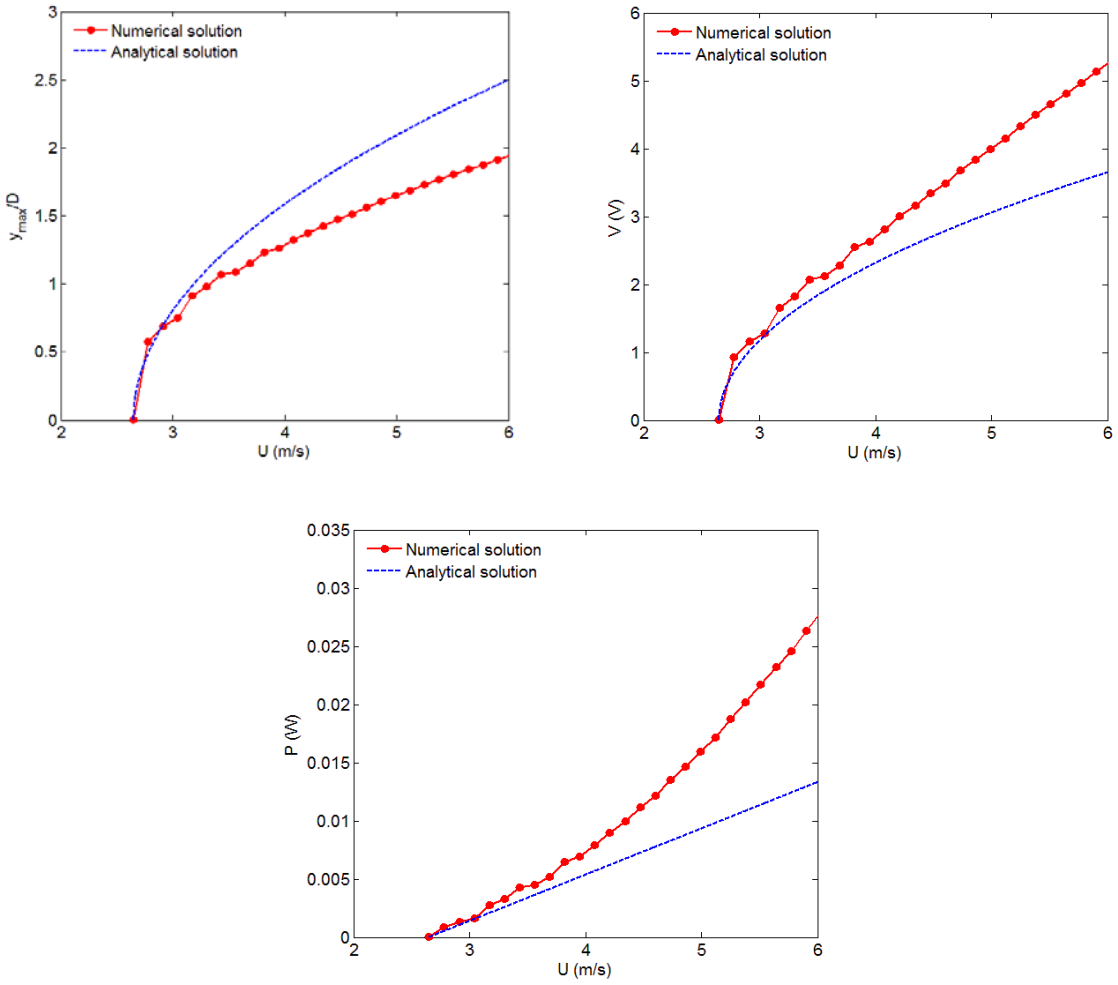

Figure 10: *Transverse displacement bifurcation diagram: Comparison between numerical prediction and analytical solution for piezoelectric triangular system when* $R = 10^3\ \Omega$ *and* $k_2 = 10000\ N/m^3$.

where $[.]_r$ and $[.]_i$ represent the real and imaginary parts, respectively. To check the validity of this nonlinear normal form solution, a comparison between the normal form predictions and numerical predictions of the governing equations is presented in Figures 10 for load resistances $R = 10^3$ and a nonlinear structural spring $k_2 = 10000N/m^3$. Clearly, the normal form of the Hopf bifurcation predicts accurately all of the amplitudes near bifurcation. Furthermore, it is clear that the type of instability is supercritical. This is expected because the real part of the effective nonlinearity α_{er} is negative. Because the normal form is applicable only near

bifurcation, it is noted that a relatively larger disagreement or discrepancy of all of the amplitudes is obtained when the wind speed is further beyond the onset speed of galloping.

3.5 Effects of the cross-sectional geometry on the onset speed of galloping

An important challenge in designing a galloping-based energy harvesting system is to select the cross-sectional geometry of the cylinder. A low U_g for onset of instability is preferred so that energy of low wind speeds can also be utilized. Linear analysis is therefore required to determine the onset speed of galloping, U_g, for various cylinder cross-section geometries. Linear part of equations (1)-(4) is written in state space formulation as given in equations (6)-(8).

State space formulation of linear part of electromechanical system reveals

$$\dot{\boldsymbol{X}} = B\boldsymbol{X}$$

where

$$B = \begin{bmatrix} 0 & 1 & 0 \\ -{\omega_n}^2 & -\left(2\xi\omega_n - \frac{\rho U D a_1}{2m}\right) & \frac{\theta}{m} \\ 0 & -\frac{\theta}{C_p} & -\frac{1}{RC_p} \end{bmatrix}$$

Clearly, the cross-sectional geometry linear parameter (a_1) affects the real and imaginary parts of the eigenvalues of matrix B. This effect is described in the plotted curves in Figure 11 which shows the variation of the onset speed of galloping U_g as a function of the electrical load resistance for four different cross-section geometries: square, isosceles triangle ($\delta = 30^o$), D section, and isosceles triangle ($\delta = 53^o$). It is observed that isosceles triangle ($\delta = 30^o$) results in a minimum wind speed U_g for all resistances amongst the four cross-sectional geometries. Barrero et al. [37] proposed formula for U_g in their work that came out to be $U_g = \frac{4m\zeta}{\rho D^2 a_1}\omega_n D$ without any energy harnessing transducer. They identified that high values of a_1 leads to low critical values of wind speed U_g whereas same is true vice versa. The aerodynamic force coefficients a_1 and a_3 for different cross-sectional geometries are given in Table 3.

Linear analysis results shown in Figure 11 and Table 4 are in excellent agreements with the results of Barrero et al. [37] which showed the isosceles triangle ($\delta = 30^o$) leads to a minimum wind to initiate galloping oscillations amongst all the other considered cross-sectional

geometries, because of highest value of a_1. A slight difference between their results with the onset speed predicted by the current linear analysis is due to the presence of the piezoelectric

Table 3: Static aerodynamics and configuration characteristics of different cross-sections

Cross-section	a_1	a_3
Square	2.3	-18
Isosceles triangle ($\delta = 30^o$)	2.9	-6.2
D-section	0.79	-0.19
Isosceles triangle ($\delta = 53^o$)	1.9	6.7

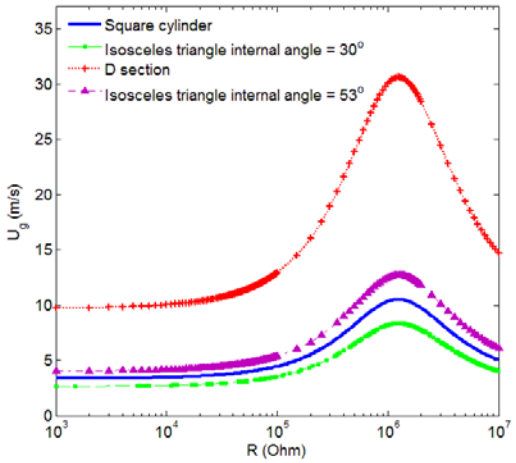

Figure 11: *Variation of the onset speed of galloping as a function of the load resistance for various cross-sectional geometries.*

material as a transducer. Therefore, isosceles triangle ($\delta = 30^o$) is the best choice for piezoelectric energy harvesting system operating at low wind velocities. They also deduced the expression for maximum efficiency of power extraction which came out to be $\eta_{max} = -\frac{a_1^2}{6a_3}$. Therefore, according to this formula D-section has a value of 0.54 followed by isosceles

($\delta = 30^o$), isosceles ($\delta = 53^o$) and square with values of 0.25, 0.09 and 0.05 respectively. This implies that although isosceles ($\delta = 30^o$) is the best choice for low wind speeds, it will not harvest as much energy as D-section at the corresponding high wind speeds. The choice of the best cross-sectional geometry at particular condition is therefore of extreme importance. To this end, in the rest of this thesis, we have focused on the triangular isosceles ($\delta = 30^o$) which is an excellent choice for nearly all practical low wind conditions.

Table 4: Variation of U_g with R for different cross-sectional geometries

$R\ (\Omega)$	$U_g(m/s)$			
	Square	Isosceles triangle ($\delta = 30^o$)	D-section	Isosceles triangle ($\delta = 53^o$)
10^3	3.345	2.6526	9.737	4.049
10^4	3.4449	2.7321	10.03	4.17
10^5	4.4414	3.5224	12.93	5.376
10^6	10.33	8.1915	30.07	12.5
1.5×10^6	10.403	8.2506	30.2873	12.59
10^7	5.066	4.0181	14.75	6.133

3.6 Summary

An electromechanical model for galloping oscillations of a triangular cylinder with piezoelectric transducer was considered. A linear analysis was performed to determine the onset speed of galloping. It was demonstrated that this critical value is strongly dependent on both the electrical load resistance and the cross-sectional geometry. The normal form of the Hopf bifurcation was derived to identify the dependence of response on the present structural and aerodynamic nonlinearities in the system as well as to characterize the type of instability. It was also shown that there is a critical value of the nonlinear structural nonlinearity in which the harvester's changes stability from subcritical to supercritical. Using the nonlinear normal form, it was

demonstrated that this nonlinear critical value strongly depends on the considered value of the electrical load resistance.

CHAPTER 4

ELECTROAEROELASTIC STABILITY

The nonlinear normal form is a very beneficial technique to characterize the type of instability and determine the influence of all available nonlinearities (structural or/and aerodynamic) on the performance of the harvester. Also, this technique is very strong in terms of designing the nonlinear springs to enhance the performance and reliability of the harvester. One of the drawbacks of the nonlinear normal form is the prediction of the stable solution in the subcritical cases for wind speed values smaller than the onset speed of galloping. In addition, it can predict the harvester's response only near bifurcation. In this section, the shooting method is used which is a very good technique that can predict all periodic solutions of autonomous and non-autonomous systems. Using this technique, our objective is to solve the equations of motion of any wind speed and any type of instability. Furthermore, we determine the eigenvalues of the monodromy matrix, termed as the Floquet multipliers, to study the stability of the periodic solutions.

4.1 Shooting method governing equations

The shooting method is one of time-domain approaches for determining periodic solutions of a system of first-order differential equations. In this approach, the initial-value problem is converted into a two-point boundary-value problem. Thus, one seeks an IC $\boldsymbol{x}(0) = \boldsymbol{\eta}$ and a solution $\boldsymbol{x}(\mathrm{t};\boldsymbol{\eta})$ with a minimal period T such that

$$\boldsymbol{x}(\mathrm{T};\boldsymbol{\eta}) = \boldsymbol{\eta} \tag{28}$$

The shooting method reduces any boundary value problem to find its equivalent IC problem. The usefulness of shooting technique resides in the fact that it takes advantage of the speed and adaptivity of initial-value problem solvers. In phase space, the trajectory that runs from $\boldsymbol{\eta}$ at $t = 0$ and reaches the same point at $t = T$ represents the required periodic solution. In shooting method, an initial guess ($T_0, \boldsymbol{\eta}_0$) is made for (T, $\boldsymbol{\eta}$) and a correction is applied until the correction reaches the desired tolerance. The correction for trajectory and time period are given $\delta\boldsymbol{\eta} = \boldsymbol{\eta} - \boldsymbol{\eta_0}$, $\delta T = T - T_0$ respectively. As a by-product of the shooting method, one can obtain the monodromy matrix and hence determine the stability of the obtained periodic solution by examining its eigenvalues, i.e. Floquet multipliers. These eigenvalues can easily quantify the local orbital divergence or convergence along a specific direction over one period of the closed orbit. Following Nayfeh and Balachandran [47], we apply this shooting method to the galloping-based energy harvester governing equations and we determine the Floquet multipliers to study the stability of the calculated solutions of the harvester. The governing equations (8),(9), and (10) of the considered energy harvester can be rewritten in the form of

$$\dot{\mathbf{X}} = \mathbf{F}(\mathbf{X}; U) \tag{29}$$

where **X** is a 3-dimensional state vector ($X_1 = \text{y}$, $X_2 = \dot{y}$, and $X_3 = V$), U is the control parameter, and **F** for our case is given by

$$\mathbf{F} = \begin{bmatrix} F_1 \\ F_2 \\ F_3 \end{bmatrix} = \begin{bmatrix} 0 & 1 & 0 \\ -\frac{k_0}{m} - \frac{k_2}{m}X_1^2 & -\left(2\xi\omega_n - \frac{\rho UDa_1}{2m} - \frac{1}{2}\frac{\rho Da_3}{mU}X_2^2\right) & \frac{\theta}{M} \\ 0 & -\frac{\theta}{C_p} & -\frac{1}{RC_p} \end{bmatrix} \begin{bmatrix} X_1 \\ X_2 \\ X_3 \end{bmatrix} \tag{30}$$

where F_1, F_2 and F_3 are the three state space equations of the considered dynamical system. Equation (29) can be rewritten as

$$\frac{\partial \boldsymbol{X}}{\partial T}(T_0, \boldsymbol{\eta_0}) = \mathbf{F}(\boldsymbol{\eta_0}; U) \tag{31}$$

To find the periodic solution, we seek

$$\delta\boldsymbol{\eta} = \boldsymbol{\eta} - \boldsymbol{\eta_0} \tag{32}$$

and

$$\delta T = T - T_0 \tag{33}$$

According to Nayfeh and Balachandran [47], the following convergence criterion

$$\mathbf{X}(T_0 + \delta T, \boldsymbol{\eta_0} + \delta\boldsymbol{\eta}) - (\boldsymbol{\eta_0} + \delta\boldsymbol{\eta}) \simeq 0 \tag{34}$$

In this analysis, the tolerance or the convergence criterion is set as $\tau = 10^{-10}$ Furthermore, the Newton-Raphson scheme is used to apply the correction for $\boldsymbol{\eta_0}$ and T, which implies

$$\left[\frac{\partial \mathbf{X}}{\partial \eta}(T_0, \boldsymbol{\eta_0}) - \mathbf{I}\right]\delta\eta + \frac{\partial \mathbf{X}}{\partial T}(T_o\,, \boldsymbol{\eta_o})\delta T = \boldsymbol{\eta_0} - \mathbf{X}(T_0, \boldsymbol{\eta_0}) \tag{35}$$

It should be noted that equation (35) is going to be solved for $\delta\boldsymbol{\eta}$ and δT and the procedure will be repeated until the condition of equation (34) is obtained. To solve the unknowns presented in equation (35), we differentiate equation (31) yields

$$\frac{d}{dt}\left(\frac{\partial \mathbf{X}}{\partial \boldsymbol{\eta}}\right) = D_{\boldsymbol{X}}\mathbf{F}(\mathbf{X}; \mathbf{U})\frac{\partial \mathbf{X}}{\partial \boldsymbol{\eta}} \tag{36}$$

Then, solving equation (36) for $\frac{\partial \mathbf{X}}{\partial \boldsymbol{\eta}}$ and replacing its obtained value in equation (35). Considering our governing ordinary-differential equations, equation (36) can

be written as

$$\frac{d}{dt}\left[\frac{\partial X}{\partial \boldsymbol{\eta}}\right] = \begin{bmatrix} 0 & 1 & 0 \\ \left(-\omega^2 + \frac{3k_2 X_1^2}{m}\right) & -\left(2\xi\omega_n - \frac{\rho U D a_1}{2m} - \frac{3}{2}\frac{\rho D a_3}{mU}{X_2}^2\right) & \frac{\theta}{M} \\ 0 & -\frac{\theta}{C_p} & -\frac{1}{RC_p} \end{bmatrix}\left[\frac{\partial X}{\partial \boldsymbol{\eta}}\right] \tag{37}$$

where

$$\left[\frac{\partial \boldsymbol{X}}{\partial \boldsymbol{\eta}}\right] = \begin{bmatrix} \frac{\partial X_1}{\partial \eta_1} & \frac{\partial X_1}{\partial \eta_2} & \frac{\partial X_1}{\partial \eta_3} \\ \frac{\partial X_2}{\partial \eta_1} & \frac{\partial X_2}{\partial \eta_2} & \frac{\partial X_2}{\partial \eta_3} \\ \frac{\partial X_3}{\partial \eta_1} & \frac{\partial X_3}{\partial \eta_2} & \frac{\partial X_3}{\partial \eta_3} \end{bmatrix}$$

To remove the arbitrariness in the phase associated with a periodic solution of an autonomous system, we consider the orthogonality condition $\mathbf{F}^{\mathrm{T}}\delta\boldsymbol{\eta} = 0$ such that the required corrections $\delta\boldsymbol{\eta}$ are normal to the vector field $\mathbf{F}$. Thus, the Newton Raphson scheme can be expressed as

$$\begin{bmatrix} \frac{\partial \mathbf{X}}{\partial \eta}(T_0, \eta_0) - \mathrm{I} & \mathbf{F}(\boldsymbol{\eta_0}; U) \\ \mathbf{F}^{\mathbf{T}}(\boldsymbol{\eta_0}; U) & 0 \end{bmatrix} \begin{bmatrix} \delta\boldsymbol{\eta} \\ \delta T \end{bmatrix} = \begin{bmatrix} \boldsymbol{\eta_0} - \mathbf{X}(T_0, \boldsymbol{\eta_0}) \\ 0 \end{bmatrix} \tag{38}$$

The ICs $\mathbf{X}(0) = \boldsymbol{\eta}$ is differentiated with respect to $\boldsymbol{\eta}$ which results in

$$\frac{\partial \mathbf{X}}{\partial \boldsymbol{\eta}}(0) = \mathbf{I} \tag{39}$$

Considering this IC relation (39), $\frac{\partial \mathbf{X}}{\partial \boldsymbol{\eta}}$ can be determined from equation (37). Furthermore, $\mathbf{F}(\boldsymbol{\eta_0}; U)$ is determined by solving equation (29). The corrections $\delta\boldsymbol{\eta}$ and δT are determined from the above equation (39) and then we check if the convergence condition is satisfied $\|\delta\eta\| < \tau$ and $\|\delta T\| < \tau$. In the case when the convergence criterion is not obtained, we update the initial guess $(T_0, \boldsymbol{\eta_0})$ to $(T_0 + \delta T, \boldsymbol{\eta_0} + \delta\boldsymbol{\eta})$and repeat the process till getting the periodic solution.

The plotted curves in Figures 12 (a) and (b) show the bifurcation diagrams of the transverse displacement when the nonlinear structural spring is set equal to 10000 N/m^3 and for two distinct values of the load resistance $R = 10^4$ and $R = 10^5\Omega$, respectively. In these curves, numerical predictions based on ode45 Runga-Kutta in Matlab, shooting method, and normal form solutions are plotted. We note that the harvester has a supercritical instability ($\alpha_{er} < 0$ when $k_2 = 10000$ N/m^3 for both considered load resistance values) and all curves are independent of the used ICs. Excellent agreement is obtained between the shooting method

predictions and the numerical predictions based on ode45 in Matlab. On the other hand, the nonlinear normal form solution has a good agreement only near the onset of bifurcation which is expected.

Based on the obtained critical values of the nonlinear structural spring in Table 2, it is clear that considering $k_2 = 10000\ \mathrm{N}/m^3$ results in the presence of subcritical instabilities for load resistance values equal to $10^6\Omega$, $1.5 \times 10^6\Omega$, and $10^7\Omega$. To this end, we plot, in Figures 13 (a), (b), and (c), the increasing and decreasing bifurcation diagrams when using ode45 in Matlab and the shooting method when k_2 = 10000N/$m^3$and R = $10^6\Omega$, $R = 1.5 \times 10^6\Omega$, and $R = 10^7\Omega$, respectively. The nonlinear normal form is not presented here because it cannot predict stable solutions for subcritical cases. Furthermore, the shooting method is also used to determine the unstable solutions and turning points. Clearly, the stable solutions and their associated hysteresis regions are well-predicted when using both ode45 and shooting method. However, ode45 Runga-Kutta cannot predict the unstable solutions and associated turning points. This analysis shows the importance of the shooting method to predict the whole behavior of the harvester (stable and unstable solutions) unlike the ode45 Runga-Kutta predictions and nonlinear normal form solutions. It follows from these plots that the hysteresis region is wider when the electrical load resistance is set equal to $1.5 \times 10^6\Omega$. This result can be explained due to the fact that the difference between the nonlinear structural spring k_2 and its associated critical value k_2^{cr} is the largest one compared to the other cases, as shown in Table 2.

To investigate in details the stability of these solutions based on the shooting method, we assume that the system exhibits a periodic solution of $\Phi(t;\boldsymbol{\eta})$ for ICs of $X(0) = \boldsymbol{\eta}$ and a periodic solution of $\Phi(t;\boldsymbol{\eta} + \boldsymbol{d_0})$ for a perturbed ICs of $\mathbf{X}(0) = \boldsymbol{\eta} + \boldsymbol{d_0}$, then the separation between the two periodic solutions at $t = T$ is given by $d(T) = \Phi\,(T;\,\boldsymbol{\eta} + \boldsymbol{d_0}) - \Phi\,(T;\,\boldsymbol{\eta})$ [32]. If the magnitude of perturbation $|\boldsymbol{d_0}|$ is small, then the separation between the two solutions can be approximated by $d(T) = \frac{\partial \Phi}{\partial \boldsymbol{\eta}}(T;\boldsymbol{\eta})\boldsymbol{d_0} = \boldsymbol{M}\boldsymbol{d_0}$. Clearly, the matrix $\boldsymbol{M}$ determines whether the initial perturbation given to the $\Phi\,(T;\,\boldsymbol{\eta})$ grows or decays with time. $\Phi(0) = \boldsymbol{\eta}$ so it implies that $\frac{\partial \Phi}{\partial \boldsymbol{\eta}}(0) = \mathbf{I}$. Therefore it is concluded that $\frac{\partial \Phi}{\partial \boldsymbol{\eta}}$ is the solution of equation (37). Consequently, the monodoromy matrix for the shooting technique is given by

$\boldsymbol{\Phi} = \frac{\partial \mathbf{X}}{\partial \boldsymbol{\eta}}(T, \boldsymbol{\eta})$. The stability of the system can easily be determined by finding the eigenvalues of this matrix, termed as Floquet multipliers.

For autonomous dynamical systems, a periodic solution is known as hyperbolic, if only one of the Floquet multipliers is located on the unit circle in the complex plane, i.e. equal to 1. We end up with a stable limit cycle or periodic attractor if all other Floquet multipliers have magnitude less than 1, whereas if all of these multipliers have magnitude greater than 1 then this would force all the neighboring trajectories to move away from the periodic solution and give unstable limit cycle or periodic repeller. On the other hand, if two or more Floquet multipliers are having a value 1, then this implies that the solution is non-hyperbolic. In this situation, a nonlinear analysis is necessary to determine the stability of this non-hyperbolic solution by testing different IC configurations and check the response of the harvester.

The shooting method solution for the considered dynamical system gives Floquet multipliers shown in Tables (5-8) for load resistance values equal to $R = 10^4$, $R = 10^6$, $R = 1.5 \times 10^6$ and $10^7 \Omega$, respectively. When $R = 10^4 \Omega$, the Floquet multipliers, presented in Table 5, indicate that a non-hyperbolic solution takes place when the wind speed is equal to the onset speed of galloping U_g. At higher wind speed, the results indicate the presence of stable limit cycle hyperbolic solutions for different wind speed values. Thus, the obtained Floquet multipliers give a complete picture about the dynamics of the harvester. These results are in very good agreement with the obtained ones based on the nonlinear normal form.

For the subcritical configurations when $R = 10^6$, $R = 1.5 \times 10^6$ and $10^7 \Omega$, Tables (6-8) present the Floquet multipliers of these configurations for different values of the wind speed. For higher values than the onset speed of galloping, stable periodic hyperbolic solution are obtained. For smaller values than the onset speed of galloping (hysteresis region), it is clear that two possible solutions are obtained. The first one indicates the presence of a stable periodic hyperbolic solution. In this case, these responses correspond to the stable branch in the hysteresis region (decreasing branch in Figures 13(a-c)). This hysteresis behavior indicates the presence a stationary point as well as a stable limit cycle for wind speeds smaller than the onset speed of instability. In addition, a sharp jump in the responses of the harvester for these load resistance values are observed at the onset speed of galloping. All of these behaviors are characteristics of a subcritical Hopf bifurcation. The second possibility indicates the presence of a non-hyperbolic

solution for different set of intermediate ICs (between the stationary point and stable limit cycle one) which correspond to the dashed branches in Figures 13(a-c).

For these non-hyperbolic solutions, a nonlinear analysis using the phase portrait technique is used to determine the stability of a non-hyperbolic solution. To this end, various intermediate IC configurations are considered, as shown in Figures 14, 15, and 16. It follows from these plots that any value of IC less than the non-hyperbolic periodic solution forces the trajectories to move to the stationary solution, whereas ICs equal to or larger than the non-hyperbolic periodic solution move to the stable limit cycle. Consequently, it is clear from these phase portrait analyses that the non-hyperbolic periodic solutions below the onset of instability are unstable and are practically impossible to achieve in reality.

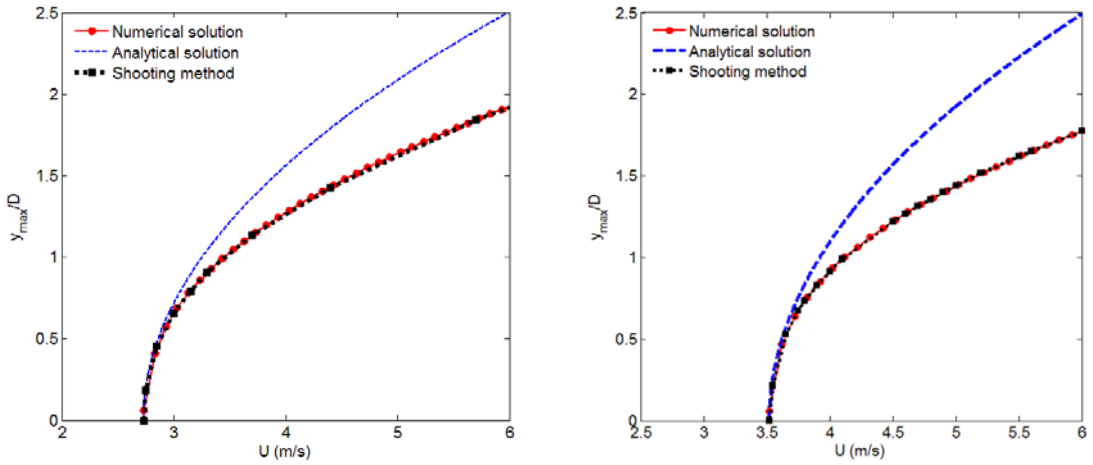

(a) (b)

Figure 12: *Bifurcation diagrams of the transverse displacement when using numerical prediction (ode45 Runga-Kutta), normal form solution, and shooting method when the nonlinear structural spring is set equal to* $k_2 = 10000\ N/m^3$ *and for two distinct values of the load resistance (a)* $R = 10^4\ \Omega$ *and (b)* $R = 10^5\ \Omega$.

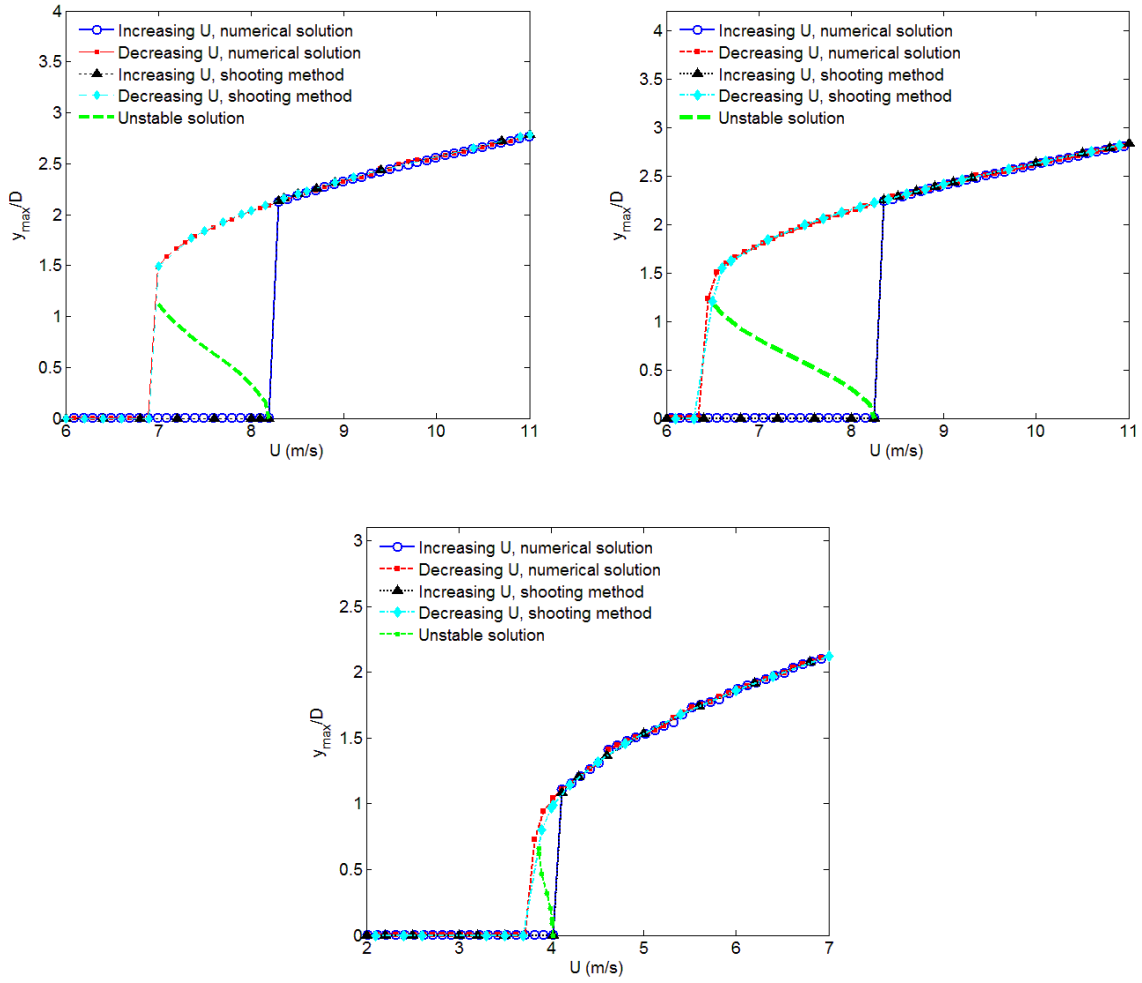

Figure 13: *Increasing/decreasing bifurcation diagrams for piezoelectric triangular system with* $k_2 = 10000\ N/m^3$ *(a)* $R = 10^6\ \Omega$ *(b)* $R = 1.5 \times 10^6\ \Omega$ *(c)* $R = 10^7\ \Omega$.

Table 5: Floquet multipliers from shooting method for triangular cylinder system for $k_2 = 10000$ N/m^3 with electric load resistance R $= 10^4$ Ω

U	Floquet multipliers
2.7321	1, 1, 0
2.75	1, 0.9923, 0
3.3	1, 0.8599, 0
3.7	1, 0.8267, 0
4.4	1, 0.0121, 0
5.7	1, 0.0534, 0

Table 6: Floquet multipliers from shooting method for triangular cylinder system for $k_2 = 10000$ N/m^3 with electric load resistance R $= 10^6$ Ω

U	Floquet multipliers
7.35 (hysteresis/high initial condition)	1, 0.9617, 0.0164
7.5 (hysteresis/high initial condition)	1, 0.95, 0.0186
7.9 (hysteresis/high initial condition)	1, 0.9181, 0.0238
8.15 (hysteresis/high initial condition)	1, 0.9087, 0.0267
7.0 (hysteresis/intermediate initial condition)	1,1,0
7.3 (hysteresis/intermediate initial condition)	1,1,0
7.6 (hysteresis/intermediate initial condition)	1,1,0
7.8 (hysteresis/intermediate initial condition)	1,1,0
8.0 (hysteresis/intermediate initial condition)	1,1,0
8.15 (hysteresis/intermediate initial condition)	1,1,0
8.1915 (onset of instability)	1, 1, 0
8.2	1, 0.9061, 0.0274
8.6	1, 0.8925, 0.0318
9.4	1, 0.7645, 0.0016
10.7	1, 0.7094, 0.0029
11.0	1, 0.6984, 0.0032

Table 7: Floquet multipliers from shooting method for triangular cylinder system for $k_2 = 10000$ N/m^3 with electric load resistance R = 1.5×10^6 Ω

U	Floquet multipliers
6.7 (hysteresis/high initial condition)	1, 0.9567, 0.0555
7.1 (hysteresis/high initial)	1, 0.9326, 0.0703
7.5 (hysteresis/high initial)	1, 0.9141, 0.0819
7.9 (hysteresis/high initial)	1, 0.9007, 0.0920
6.6 (hysteresis/intermediate initial condition)	1, 1, 0
7.0 (hysteresis/intermediate initial condition)	1, 1, 0
7.3 (hysteresis/intermediate initial condition)	1, 1, 0
7.6 (hysteresis/intermediate initial condition)	1, 1, 0
7.8 (hysteresis/ intermediate initial condition)	1, 1, 0
8.0 (hysteresis/ intermediate initial condition)	1, 1, 0
8.2 (hysteresis/ intermediate initial condition)	1, 1, 0
8.2506 (onset of instability)	1,1,0
8.4	1, 0.8800, 0.1035
8.6	1, 0.8798, 0.1079
10	1, 0.8476, 0.1347
11	1, 0.8254, 0.1518

Table 8: Floquet multipliers from shooting method for triangular cylinder system for $k_2 = 10000$ N/m^3 with resistance R = 10^7 Ω

U	Floquet multipliers
3.9 (hysteresis/high initial condition)	1, 0.9567, 0.0555
3.95 (hysteresis/ high initial condition)	1, 0.9326, 0.0703
3.99 (hysteresis/ high initial condition)	1, 0.9141, 0.0819
3.87 (hysteresis/intermediate initial condition)	1,1,0
3.95 (hysteresis/intermediate initial condition)	1,1,0
4.0 (hysteresis/intermediate initial condition)	1,1,0
4.0181 onset of instability	1, 1, 0
4.3	1, 0.8948, 0.1002
4.6	1, 0.9528, 0.6182
5.4	1, 0.8800, 0.1035
6.0	1, 0.8798, 0.1079
6.4	1, 0.8476, 0.1347
7	1, 0.8254, 0.1518

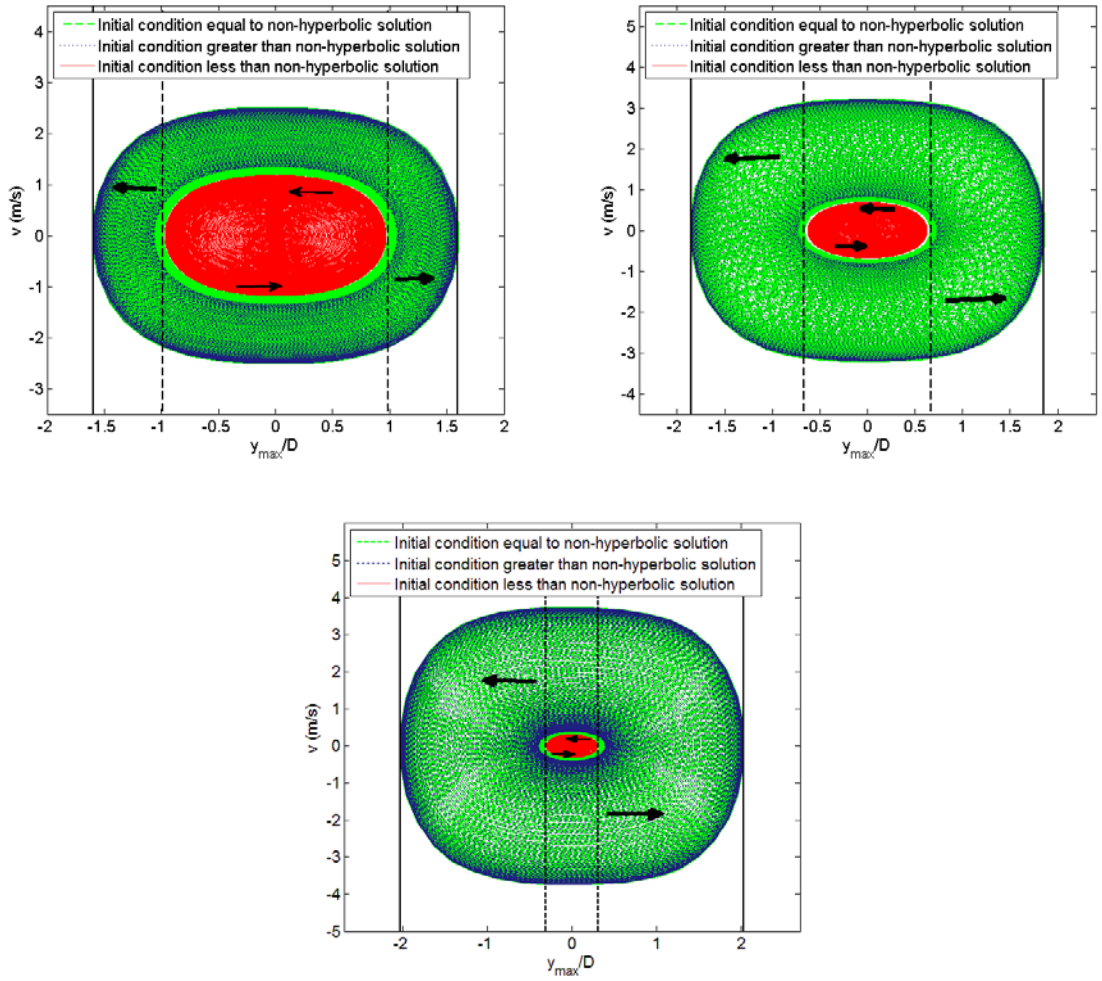

Figure 14: *Phase portraits of the non-hyperbolic solutions for different intermediate initial conditions when* $R = 10^6\ \Omega$ *and when (a)* $U = 7.1$*m/s, (b)* $U = 7.55$ *m/s, and (c)* $U = 8$ *m/s.*

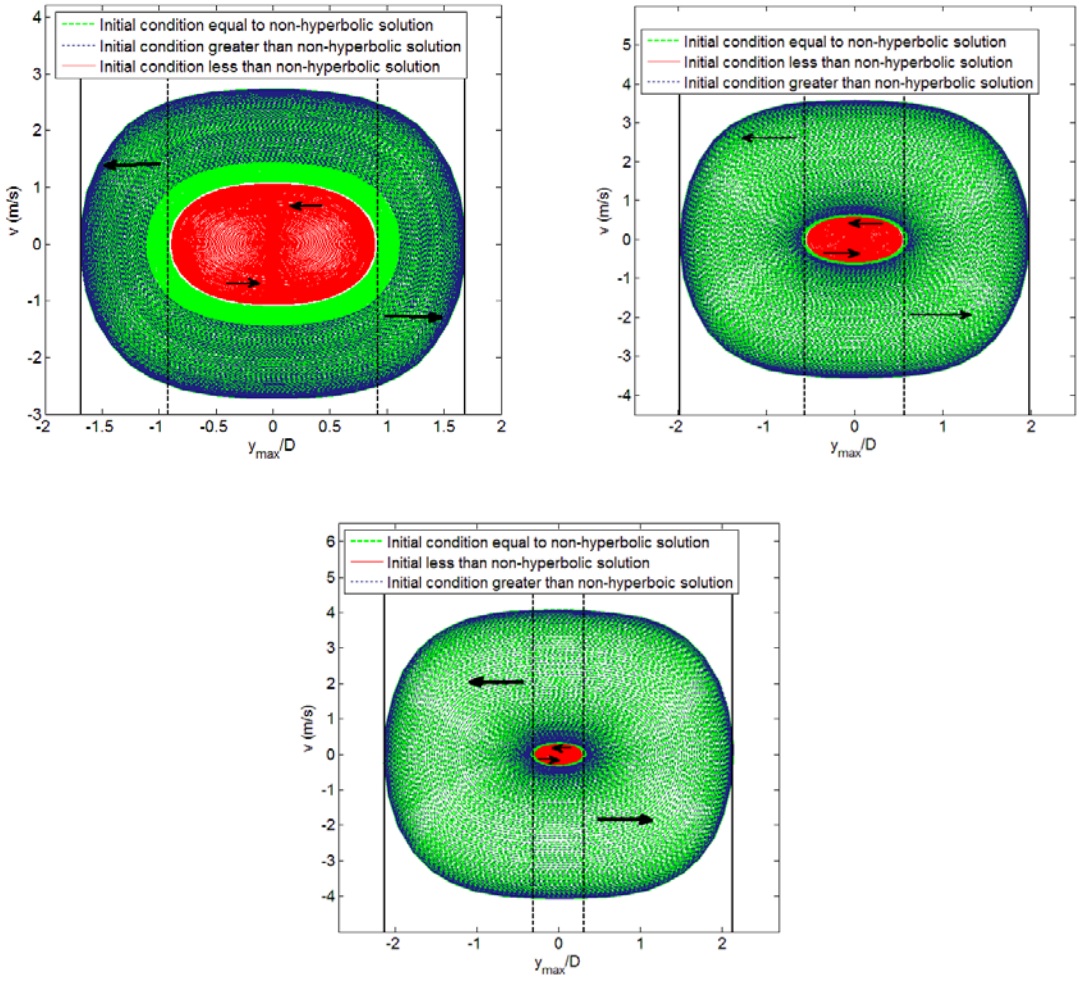

Figure 15: *Phase portraits of the non-hyperbolic solutions for different intermediate initial conditions when* $R=1.5\times10^{6}\ \Omega$ *and when (a)* $U = 6.8\ m/s$ *(b)* $U = 7.5\ m/s$ *and (c)* $U = 8\ m/s$.

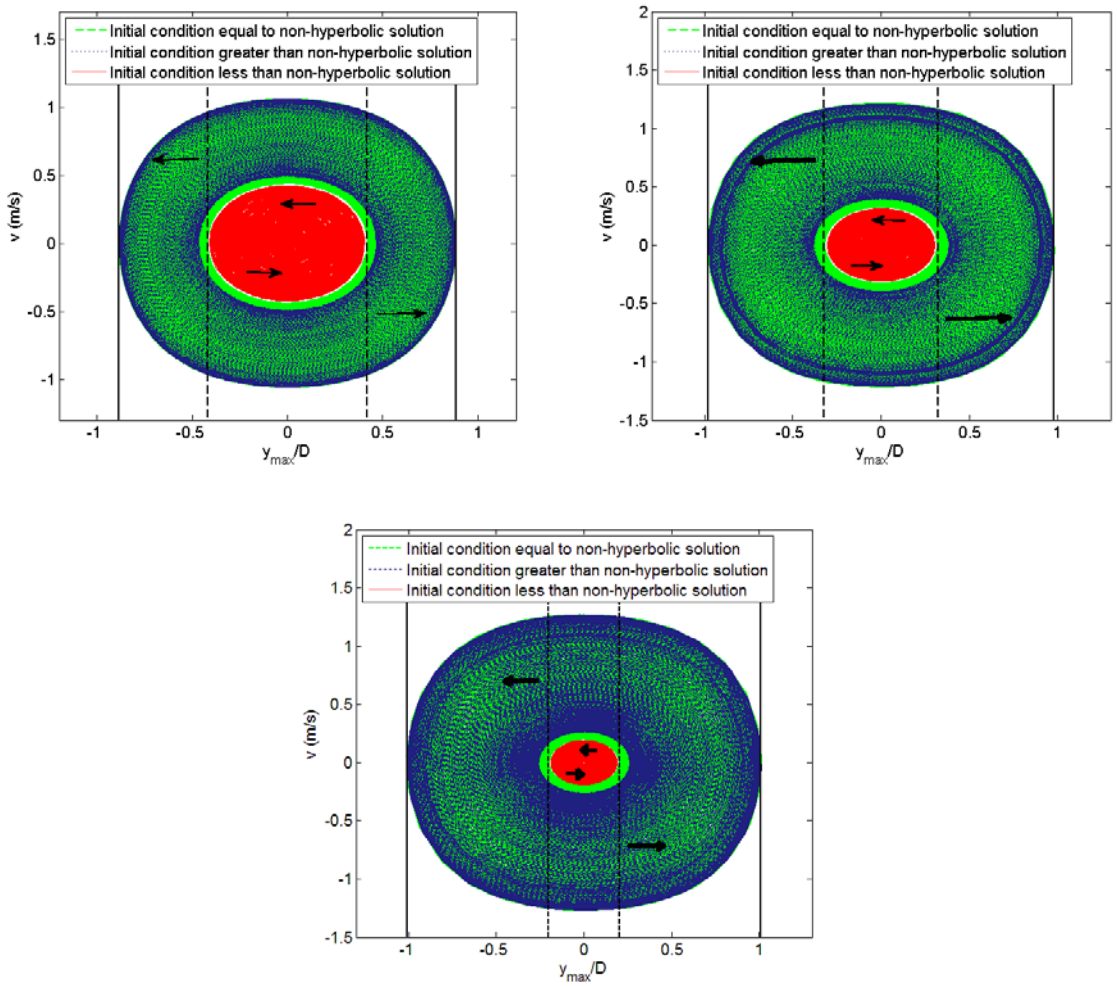

Figure 16: *Phase portraits of the non-hyperbolic solutions for different intermediate initial conditions when R=10^7 Ω and when (a) $U = 3.9$ m/s (b) $U = 3.95$ m/s and (c) $U = 3.99$ m/s*

4.2 Summary

Shooting method was used to predict the response of the considered harvester. Excellent agreement with numerical solution obtained by Runge Kutta was found. It was observed that shooting method gives the results with nearly the same accuracy as ode45 (Rung Kutta). Apart from the response depicted by ode45 in subcritical Hopf bifurcation a string of limit cycles for wind velocities less than the critical value of wind for the initiation of galloping was observed. Floquet multipliers were used to determine the stability of both the supercritical and subcritical

Hopf bifurcation responses. The former was found to be stable for all wind velocities when inspecting the Floquet multipliers. When it came to subcritical Hopf bifurcation, the string of limit cycles were identified as non-hyperbolic periodic solutions and nonlinear analysis found them to be unstable, physically impossible to achieve. The hysteresis observed in subcritical regime as well as the response after the onset of instability was found to be stable.

CHAPTER 5

CONCLUSION AND FUTURE RECOMMENDATIONS

We considered a galloping-based energy harvesting system having a piezoelectric transducer attached to it in the transverse degree of freedom. A quasi-steady approximation was used for modeling the aerodynamic lift of the cylinder whereas the Gauss law was used to couple the mechanical system with the transducer. A linear analysis was performed to determine the onset speed of galloping. It was demonstrated that this critical value is strongly dependent on both the electrical load resistance and the cross-sectional geometry. The normal form of Hopf bifurcation elaborated the dependence of response of the harvester on the aerodynamic and structural nonlinearities. This normal form was also used to calculate the critical value of the structural nonlinearity that forces the system to go from supercritical to subcritical Hopf bifurcation and vice versa. Using the nonlinear normal form, this critical nonlinear value was found to be dependent on electrical load resistance. The effects of the cross-sectional geometry on the onset speed of galloping were determined for four possible cylinder geometries. It was shown that the isosceles triangle ($\delta = 30^o$) is the most suitable cross-sectional geometry to harvest energy at low wind speed. It was also demonstrated that the D-section is the most efficient design in order to maximize the level of the harvested power. This is true for high wind speed conditions because the onset speed of galloping is too high compared to other considered configurations.

Shooting method was used to forecast the response of the considered piezoelectric harvester. Excellent consistency with numerical prediction obtained by Runge Kutta was found. It was noted that shooting method provides the results with nearly the same correctness as ode45 (Rung Kutta). Apart from the response demonstrated by ode45 in subcritical Hopf bifurcation, a succession of limit cycles for wind speeds less than the critical value of wind for the start of galloping was observed. Floquet multipliers were used to establish the stability of both the supercritical and subcritical Hopf bifurcation responses. The supercritical regime was found to be stable for all wind velocities when investigating the Floquet multipliers. For subcritical Hopf bifurcation, the streak of limit cycles were recognized as non-hyperbolic periodic solutions and nonlinear analysis revealed them as unstable, physically impossible to achieve. The response of the system after the onset of instability and the hysteresis in the subcritical regime were found to be stable.

The current research was another step closer in identifying galloping oscillations exhibited by bluff bodies a vast arena for harvesting useful energy. A vast research is still needed in terms of the controllers that should be present for controlling the galloping vibrations if wind velocities reach alarming levels in case of storms. Similarly, controllers are also needed for prohibiting the systems from entering into hysteresis region in case of subcritical Hopf bifurcations. A careful fatigue life analysis is needed for practical galloping harvesters for their long term use. Furthermore, experiments or direct numerical simulations are needed to determine the linear and nonlinear coefficients of the galloping force for other cross-section geometries. In this way, it will be easy to determine the best cross-sectional geometry.

REFERENCES

[1] Von Buren, T., "Body-Worn Inertial Electromagnetic Micro-Generators," *PhD Thesis Swiss Federal Institute of Technology Zurich, Zurich Switzerland,* 2006.

[2] Kymissis, J., Kendall, C., Paradiso, J., and Gershenfeld, N., "Parasitic power harvesting in shoes," *In the second IEEE International Conference on Wearable Computers*, 1998, pp. 132-139.

[3] Feenstra, J., Granstorm, J., and Sodano, H. A., "Energy harvesting through a backpack employing a mechanically amplified piezoelectric stack," In: *Mechanical Systems and Signal Processing,* Vol. 22, 2008, pp. 721-734.

[4] Anton, S. R., and Sodano H. A., "A review of power harvesting using piezoelectric materials (2003–2006)" *Smart Materials and Structures* Vol. 16, 2007, pp. 1–21.

[5] Cook-Chennault K. A., Thambi, N., and Sastry, A. M., "Powering MEMS portable devices-a review of non-regenerative and regenerative power supply systems with emphasis on piezoelectric energy harvesting systems," *Smart Materials and Structures* Vol. 17, 2008, pp. 043001.

[6] Yang, Z., and Yang, J., "Connected Vibrating Piezoelectric Bimorph Beams as a Wide-band Piezoelectric Power Harvester," *Journal of Intelligent Material Systems and Structures*, Vol. 20, 2009, pp. 569-574.

[7] Erturk, A., "Electromechanical modeling of piezoelectric energy harvesters," *PhD Dissertation Virginia Polytechnic Institute and State University,* 2009.

[8] Daqaq, M.F., "Response of uni-modal duffing-type harvesters to random forced excitations," *Journal of Sound and Vibration,* Vol. 329, 2010, pp. 3621–3631.

[9] Abdelkefi, A., Najar, F., Nayfeh, A. H., and Ayed, S. Ben, "An energy harvester using piezoelectric cantilever beams undergoing coupled bending–torsion vibrations," *Journal of Smart Materials and Structures*, Vol. 20, 2011, pp. 115007.

[10] Abdelkefi, A., "Global nonlinear analysis of piezoelectric energy harvesting from ambient and aeroelastic vibrations," *PhD Thesis Virginia Polytechnic Institute and State University, VA 2012*.

[11] Harne, R. L., and Wang K. W., "A review of the recent research on vibration energy harvesting via bistable systems," *Smart Materials and Structures* Vol. 22, 2013, pp. 023001.

[12] Bryant, M., Garcia, E., "Energy harvesting: a key to wireless sensor nodes," *Proceeding SPIE*, Vol. 7493, 2009, pp. 74931W.

[13] Erturk, A., Vieira, W. G. R., De Marqui, C., Inman, D. J, "On the energy harvesting potential of piezoaeroelastic systems," *Applied Physics Letters*, Vol. 96, 2010, pp. 184103.

[14] Marqui, C. D., Erturk, A., and Inman, D. J., "Piezoaeroelastic modeling and analysis of a generator wing with continuous and segmented electrodes," *Journal of Intelligent Material Systems and Structures*, Vol. 21, 2010, pp. 983–993

[15] Akaydin, H. D., Elvin, N., Andreopoulos, Y., "The performance of a self-excited fluidic energy harvester," *Smart Materials and Structures*, Vol. 21, 2012, pp. 025007.

[16] Mehmood, A., Abdelkefi, A., Hajj, M., Nayfeh, A. H., Akhtar, I., Nuhait, A. "Piezoelectric energy harvesting from vortex-induced vibrations of circular cylinder," *Journal of Sound and Vibration*, Vol. 332, Issue 19, 2013, pp. 4656-4667.

[17] Dai, H., Abdelkefi, A., Wang, L. "Theoretical modeling and nonlinear analysis of piezoelectric energy harvesting from Vortex-induced vibrations," *Journal of Intelligent Material Systems and Structures*, 2014, 1045389X14538329.

[18] Sirohi, J., Mahadik, R., "Piezoelectric wind energy harvester for low power sensors," *Journal of Intelligent Material Systems and Structures*, 2011, 1045389X11428366.

[19] Abdelkefi, A., Hajj, M. R., Nayfeh, A. H., "Piezoelectric energy harvesting from transverse galloping of bluff bodies" *Smart Materials and Structures*, Vol. 22, 015014, 2013, (11pp).

[20] Abdelkefi, A., Yan, Z., Hajj, M. R., "Nonlinear dynamics of galloping-based piezoaeroelastic energy harvesters," *The European Physical Journal Special Topics*, Vol. 222, 2013, pp. 1483-1501.

[21] Abdelkefi, A., Yan, Z., Hajj, M. R., "Modeling and nonlinear analysis of piezoelectric energy harvesting from transverse galloping", *Smart Materials and Structures*, Vol. 22, 2013, 025016 (10pp).

[22] Yang, Y., Zhao, L., Tang, L., "Comparative study of tip cross-sections for efficient galloping energy harvesting", *Applied Physics Letters*, Vol. 102(6), 2013, 064105.

[23] Bibo, A. Daqaq, M., "On the optical performance and universal design curves of galloping energy harvesters," *Applied Physics Letters*, Vol. 104(2), 2014, pp. 023901.

[24] Jung, H. J., Lee, S. W. "The experimental validation of a new energy harvesting system based on the wake galloping phenomenon," *Smart Materials and Structures*, Vol. 20(5), 2011, 055022.

[25] Abdelkefi, A., Hasanyan, A., Montgomery, J., Hall, D., Hajj, M. R., "Incident flow effects on the performance of piezoelectric energy harvesters from galloping vibrations," *Theoretical and Applied Mechanics Letters*, Vol. 4(2), 2014, 022002.

[26] Anton, S. R., and Inman, D. J., "Vibration energy harvesting for unmanned air vehicles," *Proceedings of SPIE, San Diego, CA, March*, Vol. 6982, 2008, pp. 10-13.

[27] Marqui, C. D., Erturk, A., and Inman, D. J., "An electromechanical finite element model for piezoelectric energy harvester plates," *Journal of Sound and Vibration*, Vol. 327, 2009, pp. 9-25.

[28] Katz, J. and Plotkin, A., "Low speed aerodynamics," *Cambridge University Press, Cambridge*, 2001.

[29] Benini, G. R., Belo, E. M., and Marques, F. D., "Numerical model for the simulation of fixed wings aeroelastic response," *Journal of Brazilian Society of Mechanical Sciences and Engineering*, Vol. 13, 2004, pp. 175-195.

[30] Abdelkefi, A., Nayfeh, A. H., Hajj, M. R., "Modeling and analysis of piezoaeroelastic energy harvesters," *Nonlinear Dynamics*, Vol. 67, 2011, pp. 925–939.

[31] Allen, J. J. and Smits, A. J., "Energy harvesting eel," *Journal of Fluids and Structures*, Vol. 15, 2001, pp. 629-640.

[32] Wang, D. A. and Ko, D. A., "Piezoelectric energy harvesting from flow-induced vibration," *Journal of Micromechanics and Microengineering*, Vol. 20, 2010, pp. 025019.

[33] Abdelkefi, A., Hajj, M. R., and Nayfeh, A. H., "Phenomena and modeling of piezoelectric energy harvesting from freely oscillating cylinders," *Nonlinear Dynamics.* Vol. 70, 2012, pp. 1377–88.

[34] Abdelkefi, A., Hajj, M. R, Nayfeh, A.H., "Power harvesting from transverse galloping of square cylinder," *Nonlinear Dynamics*, Vol. 70, 2012, pp. 1355-1363.

[35] Sirohi, J. and Mahadik, R., "Harvesting wind energy using a galloping piezoelectric beam," *ASME Journal of Vibration and Acoustics*, Vol. 134, 2012, pp. 1-8.

[36] Hartog, J. P. D., "Mechanical vibrations," *McGraw-Hill, New York*, 1956.

[37] Barrero-Gil, A., Alonso, G., and Sanz-Andres, A., "Energy harvesting from transverse galloping," *Journal of Sound and Vibration*, Vol. 329, 2010, pp. 2873-2883.

[38] Huesgen, T., Woias, P., and Kockmann, N., "Design and fabrication of MEMS thermo electric generators with high temperature efficiency," *Sensors and Actuators A:*, *Physical,* Vol. 145-146, 2008, pp. 423-429.

[39] Hsu, C. T., Huang, G. Y., Chu, H. S., Yu, B., Yao D. J., "An effective seebeck coefficient obtained by experimental results of a thermoelectric generator module," *Applied Energy* Vol. 88, Issue 12, 2011, pp. 5173-5279.

[40] Norman, B. C., "Power options for wireless sensor networks," In *Carnahan Conferences Security Technology*, *Proceedings 2006 40th Annual IEEE International*, pp. 17–20.

[41] Karami, M. A., "Micro-scale and nonlinear vibrational energy harvesting," *PhD Thesis*, *Virgnia Tech*, 2012.

[42] Abdelkefi, A., Barsallo, N., "Comparative modeling of low-frequency piezomagnetoelastic energy harvesters," *Journal of Intelligent Material Systems and Structures*, 1045389X14523860 (2014).

[43] S. Roundy, P.K. Wright, J. Rabaey, "A study of low level vibrations as a power source for wireless sensor nodes," *Computer communications*, Vol. 26, 2003, pp. 1131-1144.

[44] El-Hami, M., Glynne-Jones, P., White, N., Hill, M., Beeby, S., James, E., Brown, A., Ross, J., "Design and fabrication of a new vibration-based electromechanical power generator," *Sensors and Actuators A: Physical*, Vol. 92(1), 2001, pp. 335.

[45] Wang, L., Yuan, F., "Vibration Energy Harvesting by Magnetostrictive Material (MsM)," *Smart Materials and Structures*, Vol. 17, No. 4, 2008, Article Number: 045009.

[46] Parkinson, G. V. and Smith, J. D., "The square prism as an aeroelastic nonlinear oscillator," *Quarterly Journal Mechanics and Applied Mathematics*, Vol. 17, 1964, pp. 225-239.

[47] Nayfeh, A. H., Balachandran B., Applied Nonlinear Dynamics, Wiley, New York, NY, 1995.

[48] Abdelkefi, A., and Ghommem, M., "Model reduction of nonlinear aeroelastic systems experiencing Hopf bifurcation," *Journal of Modeling, Simulation, Identification, and Control*, Vol. 1, 2013, pp. 57-77.